
THE UNIVERSITY OF QUEENSLAND

AUSTRALIA

# Metal-Organic Frameworks Based Materials for Electro-Catalysis

Zongrui Jiang

Bachelor of Materials Science and Engineering

*A thesis submitted for the degree of Master of Philosophy at*

*The University of Queensland in 2019*

School of Chemical Engineering

**Abstract**

Nowadays, the growing utilisation of fossil fuel results in many environmental issues, including climate change and global warming. In order to meet energy consumption and provide sustainable resources for future generations, the development of hydrogen energy is highly desired as a renewable and clean alternative option.

Currently, some studies of hydrogen production are based on water splitting; however, the conventional method is electricity-cost that is mainly due to the sluggish kinetics of its half-reaction, oxygen evolution reaction (OER). Thus, the catalyst of OER is demanded for the ideal efficiency and rational cost of hydrogen production. Noble metals, such as ruthenium (Ru) and iridium (Ir), usually perform as the benchmark catalysts due to their high activities and good stabilities toward OER. Nevertheless, the limited reserves and extremely high costs still prevent noble-metal based materials from wide utilisation.

In this aspect, metal-organic frameworks (MOFs) can be suitable candidates for electrochemical catalysis due to their novel microstructures, atomically dispersed metal centres, and earth-abundant metal components. This thesis is focused on the design strategies of MOFs based materials in order to overcome the challenges of MOFs (e.g., poor stability and low electronic conductivity) as electro-catalysts.

Since the full coordination of metal ion in MOFs usually limits their catalytic activities, the abundant coordinatively unsaturated metal sites (CUMSs) are highly desired to improve the accessibilities of active sites with reactants. In the first part of experimental chapters, the facile microwave-induced plasma engraving is applied to fine-tune CUMSs of cobalt-based MOF (Co-MOF-74) without destroying its phase integrity by controlling plasma engraving species, intensity, and duration. The electrochemical activity of engraved MOF is found to be quantitatively correlated to the coordination geometry of metal centres corresponding to CUMSs. The developed strategy for CUMSs control and revealed CUMSs-activity correlation can inspire the further microstructure tuning of MOFs for various applications.

Furthermore, most MOFs have poor charge transferability intrinsically. In order to move beyond this shortcoming, the second part focuses on the intercalation of graphene oxide (GO) for improving

electro-catalytic activity. Graphene is well known for its one-atom thickness and high conductivity. The epoxy groups located on GO surface are able to achieve a strong connection with MOFs. Thus, this study successfully synthesised Co-MOF-74/GO composites with hierarchical structure. The composite with optimised loading proportion of GO exhibited enhanced charge transferability and OER performance.

**Declaration by author**

This thesis is composed of my original work, and contains no material previously published or written by another person except where due reference has been made in the text. I have clearly stated the contribution by others to jointly-authored works that I have included in my thesis.

I have clearly stated the contribution of others to my thesis as a whole, including statistical assistance, survey design, data analysis, significant technical procedures, professional editorial advice, financial support and any other original research work used or reported in my thesis. The content of my thesis is the result of work I have carried out since the commencement of my higher degree by research candidature and does not include a substantial part of work that has been submitted to qualify for the award of any other degree or diploma in any university or other tertiary institution. I have clearly stated which parts of my thesis, if any, have been submitted to qualify for another award.

I acknowledge that an electronic copy of my thesis must be lodged with the University Library and, subject to the policy and procedures of The University of Queensland, the thesis be made available for research and study in accordance with the Copyright Act 1968 unless a period of embargo has been approved by the Dean of the Graduate School.

I acknowledge that copyright of all material contained in my thesis resides with the copyright holder(s) of that material. Where appropriate I have obtained copyright permission from the copyright holder to reproduce material in this thesis and have sought permission from co-authors for any jointly authored works included in the thesis.

**Publications included in this thesis**

**Zongrui Jiang,** Lei Ge, Linzhou Zhuang, Mengran Li, Zhanke Wang, and Zhonghua Zhu, Fine-tuning the coordinatively unsaturated metal sites of metal-organic framework by plasma engraving for enhanced electro-catalytic activity. *ACS Appl. Mater. Interfaces* **2019**.

**-incorporated as Chapter 4.**

| Contributor | Statement of Contribution |
|---|---|
| Author Zongrui Jiang | Concept and design (70%)<br>Analysis and interpretation of data (70%)<br>Drafting and writing (75%) |
| Author Lei Ge | Concept and design (10%)<br>Analysis and interpretation of data (5%)<br>Drafting and writing (10%) |
| Author Linzhou Zhuang | Analysis and interpretation of data (10%)<br>Drafting and writing (5%) |
| Author Mengran Li | Analysis and interpretation of data (5%) |
| Author Zhanke Wang | Analysis and interpretation of data (5%) |
| Author Zhonghua Zhu | Concept and design (20%)<br>Analysis and interpretation of data (5%)<br>Drafting and writing (10%) |

**Submitted manuscripts included in this thesis**

No manuscripts submitted for publication.

**Other publications during candidature**

Linzhou Zhuang, Lei Ge, Hongli Liu, **Zongrui Jiang,** Yi Jia, Zhiheng Li, Dongjiang Yang, Rosalie K. Hocking, Mengran Li, Longzhou Zhang, Xin Wang, Xiangdong Yao, Zhonghua Zhu, A Surfactant‐Free and Scalable General Strategy for Synthesizing Ultrathin Two‐Dimensional Metal–Organic Framework Nanosheets for the Oxygen Evolution Reaction. *Angew. Chem. Int. Ed.* **2019**, 58, 13565.

**Contributions by others to the thesis**

Prof. Zhonghua (John) Zhu, Dr. Lei Ge had significant contributions on the research and writing presented in this thesis. The staff of the Australian Microscopy and Microanalysis Research Facility at the Centre for Microscopy and Microanalysis at The University of Queensland are acknowledged for technical assistance and precious suggestions. Dr. Rosalie K. Hocking helped with the XAS tests in the Australian Synchrotron Facility and the analysis of XAFS data.

**Statement of parts of the thesis submitted to qualify for the award of another degree**

No works submitted towards another degree have been included in this thesis.

**Research Involving Human or Animal Subjects**

No animal or human subjects were involved in this research.

**Acknowledgements**

I am more than grateful for all the support from my supervisors, Prof. Zhonghua (John) Zhu and Dr. Lei Ge. Their insightful guidance and immense knowledge always encourage me to widen my research from diverse perspectives. It would not be possible to accomplish this project without their intensive suggestions.

I would like to thank all the people in the labs for their patient and reliable supports, in any respect as follows: Dr. Mengran Li, Mr. Linzhou Zhuang, Mr. Zhanke Wang, Mr, Zhiheng Li, Dr. Shuai Gao, Dr. Rijia Lin, Dr. Xiaoyong Xu, Dr. Byron Villacorta, Mr. Sathia Aruliah, Dr. Raj Ratnaraj, Mr. Shirjeel Khan, Mr. Ateeq Rehman, Mr. Abdulwadood Babikir, Mr. Jinxuan Zhang, Dr. Fengli Liang, Dr. Wei Zhuang, Dr. Jie Zhao, and all the group members.

A very special gratitude goes out to all the scientific and technical assistance in the Australian Microscopy and Microanalysis Research Facility at the Centre for Microscopy and Microanalysis at The University of Queensland. I sincerely appreciate the kind help from Dr. Barry Wood, Ms Ying Yu, Dr. Kim Sewell, Mr. Ron Rasch and Ms. Anya Yago. The Australian Synchrotron Facility and Taiwan National Synchrotron Radiation Research Centre are highly appreciated for the XAS tests and data analysis.

And finally, last but by no means least, my appreciation must goes to my parents and friends for supporting me throughout this project and all my life.

**Financial support**

No financial support was provided to fund this research.

**Keywords**

electro-catalysis, metal-organic frameworks, oxygen evolution reaction, coordinatively unsaturated metal sites, plasma engraving, graphene oxide intercalation

**Australian and New Zealand Standard Research Classifications (ANZSRC)**

ANZSRC code: 091205, Functional Materials, 60%

ANZSRC code: 090403, Chemical Engineering Design, 20%

ANZSRC code: 091202, Composite and Hybrid Materials, 20%

**Fields of Research (FoR) Classification**

FoR code: 0912, Materials Engineering, 80%

FoR code: 0904, Chemical Engineering, 20%

# Table of Contents

# List of Figures

# List of Tables

# List of Abbreviations

OER – Oxygen evolution reaction

MOFs – Metal-organic frameworks

CUMSs – Coordinatively unsaturated metal sites

GO – Graphene oxide

HER – Hydrogen evolution reaction

TOF – Turnover frequency

BET – Brunauer-Emmett-Teller

ZIF – Zeolitic imidazolate framework

NCNFs – N-doped carbon nanotube frameworks

ADT – Accelerated durability test

CoP – Cobalt phosphide

CNTs – Carbon nanotubes

XPS – X-ray photoelectron spectra

POM – Polyoxometalate

BTC – Benzene-1,3,5-tricaboxylate

INA – Isonicotinic acid

BDC – Benzenedicarboxylic acid

TCPP – Tetrakis (4-carboxyphenyl) porphyrin

RHE – Reversible hydrogen electrode

PVP – Polyvinylpyrrolidone

PFH – Perfluorohexane

DBD – Dielectric barrier discharge

$H_4$dobdc – 2-5-dihydroxyterephthalic acid

DMF – N,N-dimethylformamide

LSV – Linear sweep voltammetry

RDE – Rotating disk electrode

XRD – X-ray diffraction

SEM – Scanning electron microscope

TEM – Transmission electron microscope

FTIR – Fourier-transform infrared spectroscopy

BJH – Barrett Joyner Halenda

XAS – X-ray absorption spectra

ORR – Oxygen reduction reaction

SALE – Solvent-assisted ligand exchange

EDX – Energy dispersive X-ray

XANES – X-ray absorption near edge structure

EIS – Electrochemical impedance spectroscopy

FT-EXAFS – Fourier transforms of the $k^3$-weighted extended X-ray absorption fine structure

# Chapter 1. Introduction

### 1.1. Background

Recently, global energy demand is increasing rapidly. As a consequence, the growing utilisation of fossil fuel leads to many environmental issues such as the greenhouse effect and air pollution. Enormous carbon dioxide is released by fossil fuel concentrating heat under atmosphere and results in global warming. Other exhaust gases, like sulfur dioxide and nitrogen dioxide, are inhaled by humans and cause health complications. In order to meet energy consumption and provide a sustainable environment, scientists are focusing on the research of renewable and clean energy. Hydrogen is exactly the energy which corresponds these standards and has the potential to be developed for the future.

Among all the elements on the earth, hydrogen is the most common one that can be extracted from water, and its ideal emission after consuming this energy is still water. Thus, hydrogen is the cleanest one with relativity high energy density among various new generation energies. The renewable, non-poisonous exhaustion and other ideal properties make hydrogen plays an important role in the future. However, there are still some challenges on the application of this energy, such as its unstable condition and storage complications. At the first place, a valid and relatively cheap method of hydrogen generation must be achieved.

Currently, some methods of hydrogen production are mainly based on steam-methane reforming or harnessing from fossil fuel.[1] They will still lead to pollution issues and the production are limited by other scarce sources. Other methods are established on the reaction of water splitting, that is separated into two half-reactions, oxygen evolution (OER) and hydrogen evolution reaction (HER). However, the conventional method is electricity-cost and inefficient which is mainly due to the sluggish kinetics of OER.

Thus, the catalysts for OER need to be achieved in order to produce hydrogen with high efficiency and rational cost. Metal-organic frameworks (MOFs) can be suitable candidates for electro-catalysis due to their novel structures, high surface area and controllable components.[2] More important, they can be improved by designed strategies, such as morphology control, plasma engraving or hybridisation, to fine-tune the microstructure for further enhanced catalytic activities in OER and other chemical reactions.

### 1.2. Research scope and contributions

This thesis mainly focuses on the route designing of MOFs based electrocatalysts and the mechanism understanding of their microstructure modulation. The intrinsic challenges of cobalt MOF (Co-MOF-74) are overcome through applying derived strategies so that the high-performance and cost-effective catalysts can be achieved. The objectives of this research are shown as follows:

- To fine-tune coordinatively unsaturated metal sites (CUMSs) on MOF surface for sufficiently exposing active metal centres during electro-catalysis.
- To demonstrate the correlation between coordination geometry and electro-catalytic activity.
- To intercalate graphene oxide (GO) in MOF for improving charge transferability and developing high-performance hybrid catalysts.

### 1.3. Thesis structure

**Chapter 1. Introduction**

The research background, pursuing objectives and outline of this thesis are given in this chapter.

**Chapter 2. Literature Review**

In this chapter, the fundamentals of catalysis reaction at the beginning of the literature review. Thereafter, variously reported catalysts are presented for the application of this research. Finally, different strategies for designing MOF based catalysts are summarised with their benefits and limitations. Two promising routes are concluded to implement as the methods for this thesis in the following sections.

**Chapter 3. Research Method**

This chapter lists all the chemicals sources and synthesis methods in the study. It also describes all the utilised equipment and procedures, including plasma engraving, electro-catalytic measurement and materials characterisations.

**Chapter 4. Fine-tuning the Coordinatively Unsaturated Metal Sites of MOF by Plasma Engraving for Enhanced Electro-catalytic Activity**

Microwave-induced plasma engraving is investigated on MOF under designed conditions. The structure and electrochemical performance characterisations are performed, which reveals the quantitative correlation between coordination geometry and electro-catalytic activity. The content of this chapter has been published on the ACS Applied Materials & Interfaces (DOI: 10.1021/acsami.9b15794).

**Chapter 5. Enhancing Electro-catalytic Activity of Cobalt-based MOF Electrocatalysts with Graphene Oxide Intercalation**

In order to benefit from the synergistic effect of high conductivity materials, the route of GO intercalation is paved to fabricate MOF/GO composites with a hierarchical structure. Notably, the sample with the highest loading proportion exhibits enhanced charge transferability and performance on OER.

## Chapter 6. Conclusion and Proposal for Future Works

The content in this chapter summarises all the findings and contributions in this thesis. The proposal of future work is also given to further investigate the design of scalable and effective electro-catalysts.

# Chapter 2. Literature Review

## 2.1. Fundamentals of oxygen evolution reaction (OER)

### 2.1.1. Reaction mechanism

Water splitting is a rational way to produce hydrogen energy due to its clean emission and abundant resource. The water can be separated into oxygen and hydrogen under high electric current, and the electricity can be generated from renewable sources (e.g. solar or wind). Nevertheless, its cost by the conventional method is quite expensive, because the current needs to overcome a potential energy barrier and active water molecule for splitting (the reaction is shown in Equation 1).

**Equation 1.** Water splitting:

$$H_2O \rightarrow H_2 + \frac{1}{2}O_2$$

Therefore, the reaction of water splitting should be considered and researched for higher efficiency, which means the electrocatalysts are required on the massive production of hydrogen. Considering the mechanism, water splitting can be divided into two half-reactions, that are oxygen evolution reaction (OER) and hydrogen evolution reaction (HER). Although both of them can be catalysed, OER has more sluggish kinetics than HER due to the four-electron process.[1, 3] Thus, OER will be focused in the following sections. The reaction equations under alkaline condition are shown in Equation 2.

**Equation 2.** OER under alkaline condition:

$$M + OH^- \rightarrow MOH + e^-$$

$$MOH + OH^- \rightarrow MO + H_2O + e^-$$

$$MO + OH^- \rightarrow MOOH + e^-$$

$$MOOH + OH^- \rightarrow M + O_2 + H_2O + e^-$$

where “M” refers to the active site of the catalyst. As an ideal catalyst, the active site should have an applicable bond, because it needs to be sufficiently strong to absorb $OH^-$ and weak to release $O_2$. Meanwhile, the change of Gibbs free energy after the formation of “MOH”, “MO” and “MOOH” should be minimised with an optimal catalyst. Among them, the formation of MOOH from MO on the active site surface is the hardest step due to the requirement of uphill free energy at equilibrium

potential. Thus, an extra potential must be applied to achieve OER with conventional electrodes, and catalysts aim to decrease this high potential in order to move the equilibrium positively.

### 2.1.2. Evaluating parameters

#### Onset potential and overpotential

According to the above section, onset potential is very critical to describe the performance of a catalyst. However, it is hard to measure the value accurately when the reaction just happens. In this case, overpotential shows the difference between the applied potential at the certain current density and standard potential for the reaction, and thus it is usually used to compare catalytic activities of various catalysts. Generally, a catalyst with overpotential between 300 - 400 mV at 10 mA $cm^{-2}$ is regarded as a good choice for OER.

#### Tafel slope

Evolving from Butler-Volmer equation, the Tafel relationship can be revealed in Equation 3.

**Equation 3.** Tafel slope calculation:

$$\eta = b \cdot \log (j/j_0)$$

where $\eta$ is the overpotential, b is the Tafel slope, j is the applied current density and $j_0$ is the exchange current density of forward and reverse reaction at equilibrium potential. As a result, the Tafel slope describes the linear relationship between overpotential and logarithm of current density. It helps to exhibit reaction kinetics and compare various catalysts.

#### Turnover frequency (TOF)

The TOF is calculated by the following Equation 4:

**Equation 4.** Turnover frequency calculation:

$$\mathrm{TOF} = \frac{j \times A_{geo}}{4 \times F \times n}$$

where $A_{geo}$ is the geometric area of working electrode, 4 is the number of transferring electrons in OER, F is the Faraday constant (96,485 C $mol^{-1}$) and n refers to the number of moles of total active sites in the catalyst. The TOF in this project shows the frequency of OER per active site at a certain

overpotential. The active sites for the catalysts this research are assumed as the cobalt atoms and the moles of cobalt atoms are estimated through the molecular formula of MOF.

**Electrolyte**

In addition to the properties of catalysts, variety electrolytes will also influence their performance on water splitting due to their different pH values. Most electrocatalysts for OER work favourably in the alkaline environment but hardly maintain their structures in the acidic environment.[4] Therefore, a catalyst is desirable to be fabricated for well working under the full range of pH from 0 to 14.

### 2.1.3. Key factors of catalysts to enhance electro-catalytic activity

In order to improve the performances of major catalysts on electrochemical reactions, scientists are focusing on the intrinsic activity and the accessibility of active sites. In the case of water splitting, the intrinsic activity of the catalyst can be determined by the components, valence states, charges transferability, etc. Meanwhile, the accessibility generally depends on the morphology and microstructure. These key factors of catalysts must be revealed to determine the objectives and hypothesis of researches.

As to improve intrinsic activities of catalysts, for example, Tang and co-workers have composited a polyoxometalate-based (POM-based) MOF with graphene. Due to the synergistic effect, its conductivity could be increased by forming hybrid catalysts.[1, 5] In result, the hybrid material showed an outstanding HER activity with small onset potential (close to 20% of Pt/C catalyst at the same testing condition) and high current density.[6] Besides, bimetallic catalysts can also improve the performance from monometallic materials.[7] Huang et al. used Zn, Ni and Cu as a second metal element on Co-based bimetallic sulphide polyhedral, and they showed higher activities on HER than $Co_3S_4$ due to the homo-incorporation.[8]

In the case of optimising accessibilities, the morphology modification can significantly increase Brunauer-Emmett-Teller (BET) surface area, which allows more active sites to be exposed to reactants. For instance, Yu-xia Bao and co-workers used zeolitic imidazolate frameworks-67 (ZIF-67) as a precursor to synthesis N-doped carbon nanotube frameworks (NCNFs).[9] ZIF-67 provided carbon and nitrogen sources for NCNFs growth and became a template for the formation of hollow structures. As a result, the BET surface area was increased by 2.5 times than ZIF-67. This hollow

framework showed enhanced activity and stability even compared with commercial Pt/C electro-catalyst for OER and ORR.

Another interesting find is that the synthesis strategy of low-dimension catalysts also makes it possible to increase the surface area. The modulator-assisted methodology was used to achieve MOF nanorods and nanoribbons with excellent charge transferability.[10] MOF-74 was tailored into rod-shaped morphology due to the cooperation of salicylic acid as a modulator. After KOH-assisted sonochemical treatment, the graphene nanoribbons could be obtained. The exfoliated material exhibited an enhanced surface area (411 $m^2$ $g^{-1}$), which might be attributed to the well-organised arrangement of MOF precursor. As a result, the nanorods showed fast charge transport velocity, and the nanoribbons had good super-capacitor performance.

When it comes to the microstructure, MOFs have the outstanding feature since their atomically dispersed metal centres are recognised as active sites for the electro-catalysis toward OER.[1, 11] However, the full coordination of metal centres in MOFs usually limit their direct applications as electrocatalysts.[11b, 12] For example, the cobalt atoms in zeolitic imidazolate frameworks (e.g. ZIF-67) were fully coordinated by nitrogen atoms and connected with imidazole ligands.[13] In this case, the electro-catalytic application of ZIF-67 was not satisfying due to the lack of exposing metal sites.[14] In contrast, the MOFs (e.g. metal-benzenedicarboxylic acid nanosheets,[12] MIL-101[15] and cobalt dithiolene[16]) with a multitude of CUMSs displaying superior electro-catalytic activities.[11b, 14] Therefore, optimising the density of CUMSs is an essential strategy for developing MOFs to enhance electro-catalytic performance so that abundant active sites can be accessed by reactants.

### 2.2. Materials screening for oxygen evolution reaction

In order to build catalysts with desired properties, the nanoscale porous material becomes a good choice. Currently, some catalysts have been achieved from precious metals, such as ruthenium, platinum or iridium.[1] They can reduce the overpotential and speed up the reactions in both acidic and alkaline environments without consuming themselves. However, the challenge is that some of them are too expensive and scarce to be applied to massive fabrication, and others still have the potential to be further tailored for enhancing activities. The following are brief instructions of some typical catalysts which have been achieved previously.

#### 2.2.1. Noble-metal based catalysts

Noble metals, such as ruthenium (Ru), palladium (Pd), iridium (Ir) and platinum (Pt), usually have high resistance to corrosion and oxidation.[17] Thanks to their outstanding performances toward OER, a great number of researchers focused on their alloys, oxides or composites.[4] Among the noble metals, Ru and Ir oxides are always regarded as standard criteria for other catalysts on OER due to their low onsite potentials and Tafel slopes.[18] According to the research, $RuO_2$ and $IrO_2$ showed low overpotential (approximately 370 mV and 560 mV respectively).[19] In order to further improve the performances, these noble-metal had been studied in nanoscale and Ir nanoparticles exhibited high activity and durable stability.[20] However, the limited reserves and extremely high costs still prevent noble-metal based materials from wide utilisation.

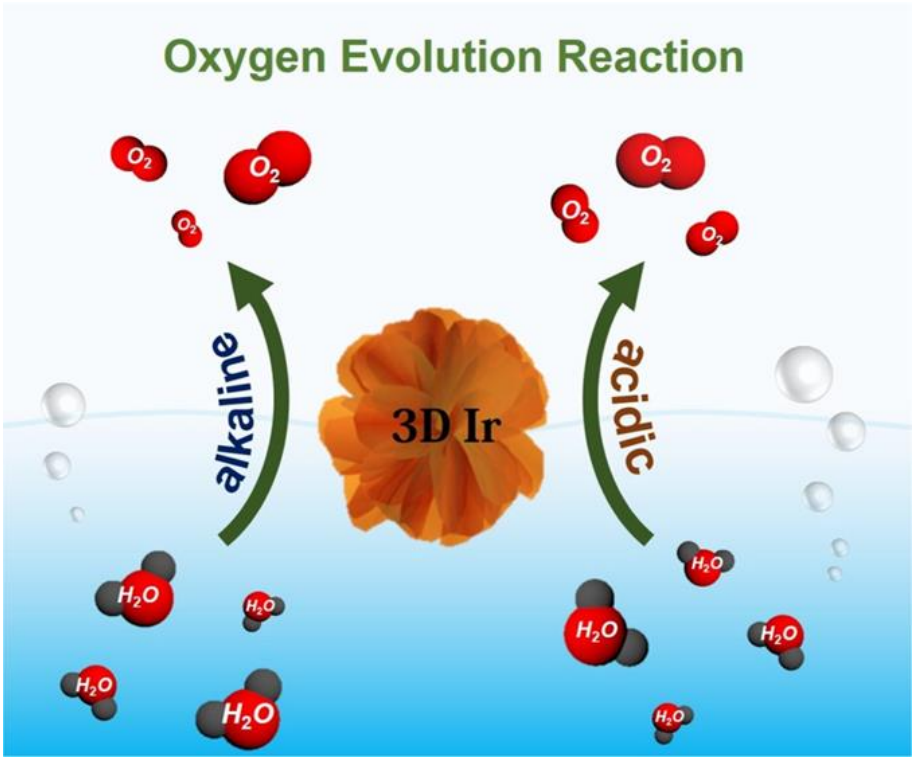


**Figure 2-1.** The schematic illustration of Ir superstructure as oxygen evolution electrocatalysts in broad pH range.[18] Reproduced with permission from ref [18]. Copyright 2016, American Chemical Society.

### 2.2.2. Abundant-metal based catalysts

In the past decades, abundant-metals have attracted plenty of attention from scientists because of their low costs, wide applications and durable stabilities.[4] These metals, like cobalt (Co), nickel (Ni), iron (Fe) and manganese (Mn), have been used with different chalcogen compounds. Here are some examples of their applying details.

#### Metal oxides

In the case of electro-catalytic reactions, the metal oxides would be extremely suitable due to the multivalent oxidation states of metal atoms as the active sites for OER. $CoO_x$, for example, is a series of oxides with many practical applications by the reason of variety valence states of Co (2+, 3+ and 4+).[21] In the previous research, amorphous metal oxides films were achieved by photochemical metal-organic deposition.[22] Compared with other conventional fabrication methods, this low-temperature fabrication technique led to a uniform distribution of metal atoms and prevented films from phase segregation. The outcomes of amorphous $FeO_x$ and $CoO_x$ were demonstrated with the Tafel slopes about 40 mV $dec^{-1}$.

Furthermore, the synergistic effect was able to enhance electro-catalytic activities by doping various metals in oxides.[21, 23] For instance, Sn and Ni cation-doped $Co_3O_4$ catalysts showed higher charge transferability and lower overpotential than pristine oxide. The flexible and controllable composition of perovskite oxides also helped them to get attention in many application fields.[24] The common formula of perovskite is $ABO_3$ where A is alkaline-earth metal and B is transition metal. Recently, they were also reported of high catalytic activity on OER in alkaline condition. Thanks to the intermediate spin state of Co cations, $Ba_{0.5}Sr_{0.5}Co_{0.8}Fe_{0.2}O_{3-\delta}$ (BSCF) had remarkable intrinsic activity even compared with Ir oxide catalysts.[24c] Zhu and co-worker had fabricated P-doped perovskite oxide, $SrCo_{0.95}P_{0.05}O_{3\delta}$ (SCP), with a tetragonal superstructure.[24a] The electric conductivity played an important role in OER activity and was increased due to the small amount of phosphorus doping. The stable tetragonal structure improved its durability by preventing Sr ions from considerable leaching. Interestingly, the activity of SCP was enhanced during accelerated durability test (ADT) which might be contributed to the formation of A-site-deficient structure.

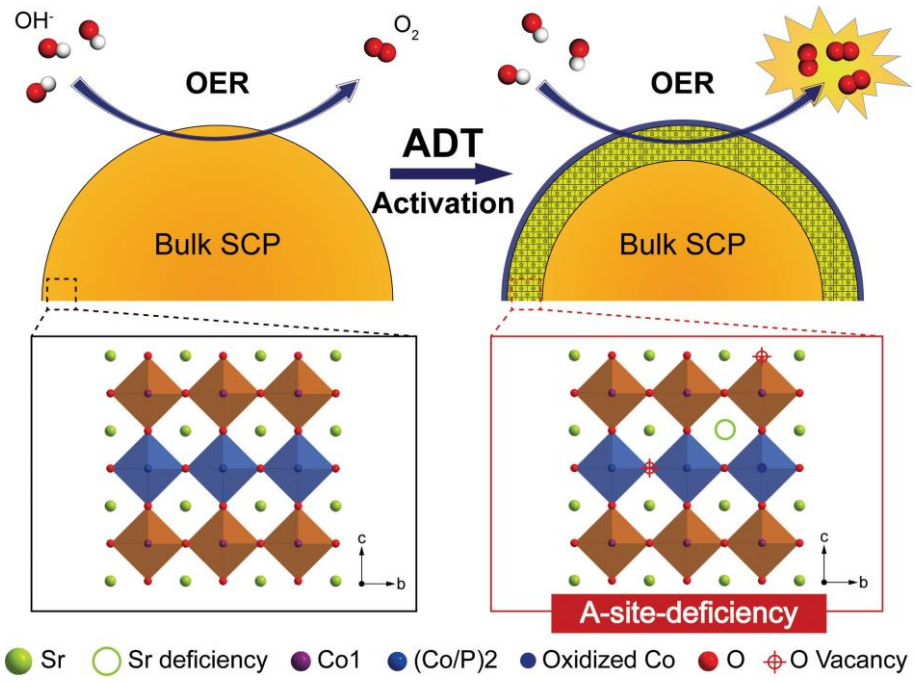


**Figure 2-2.** Schematic illustration of the ADT activation for SCP catalyst.[24a] Reproduced with permission from ref [24a]. Copyright 2016, John Wiley and Sons.

### Metal phosphides/phosphates

Earth-abundant-metal phosphides and phosphates have been studied on water splitting because of

their outstanding activities and stabilities. For instance, Ryu and co-workers investigated in the catalytic performance of cobalt phosphide (CoP) nanoparticles.[25] In the same year, a CoP mesoporous material was fabricated through electrodeposition synthesis method.[26] As shown in Figure 2-3, CoP nanorods grew on the Ni foam by potentiostat electrodeposition where Ni foam had high conductivity to ensure applicable charge transferability. Meanwhile, the further nucleation while nanorods forming led to mesoporous generation inside. Thus, the material could even compete with commercial catalysts in alkaline condition and achieve overpotential of 390 mV at a current density of 10 mA $cm^{-2}$.

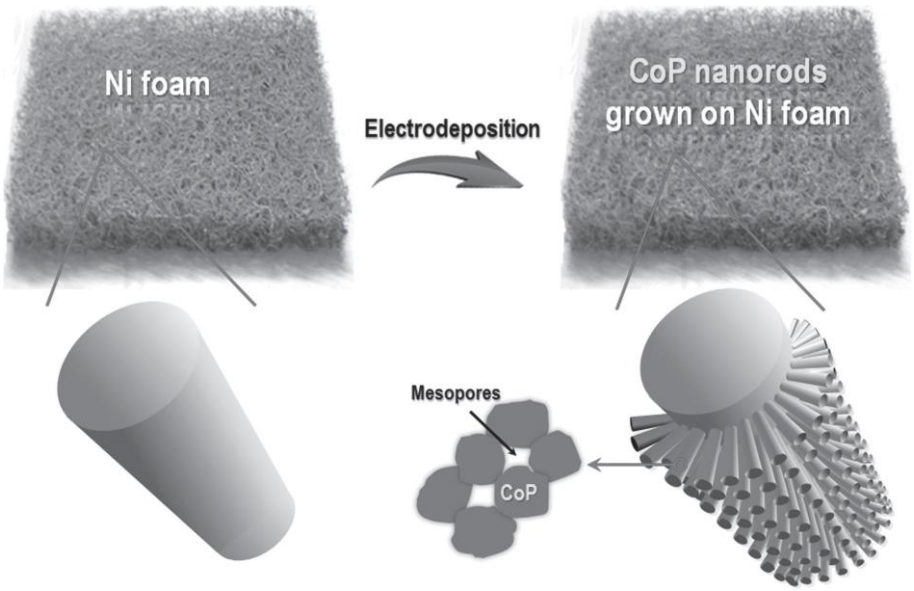


**Figure 2-3.** Fabrication scheme of Co-phosphide mesoporous material.[26] Reproduced with permission from ref [26]. Copyright 2015, John Wiley and Sons.

According to the research of Dutta, a substrate with good conductivity was needed while phosphide materials formation.[27] Chang et al. mechanically mixed CoP nanorod-based material with conductive carbon and the product showed enhanced activity (320 mV at 10 mA $cm^{-2}$).[28] Furthermore, ultrafine CoP nanoparticles had been achieved on carbon nanotubes (CNTs) by Hou and co-workers.[29] The synthesis methodology was based on $Co_3O_4$-CNT composite and the OER performance was also comparable with $Co_3O_4$ and CoP. Its low overpotential of 330 mV at 10 mA $cm^{-2}$ and Tafel slope of 50 mV $dec^{-1}$ exhibited the superior catalytic activity. Via the similar fabrication method, FeP porous nanorods had been achieved on CNT backbones with advantageous structural features (Figure 2-4).[30] The hierarchical nano-material led to a remarkable activity which required

overpotential of 300 mV at 10 mA $cm^{-2}$ and Tafel slope of 53 mV $dec^{-1}$ on OER.

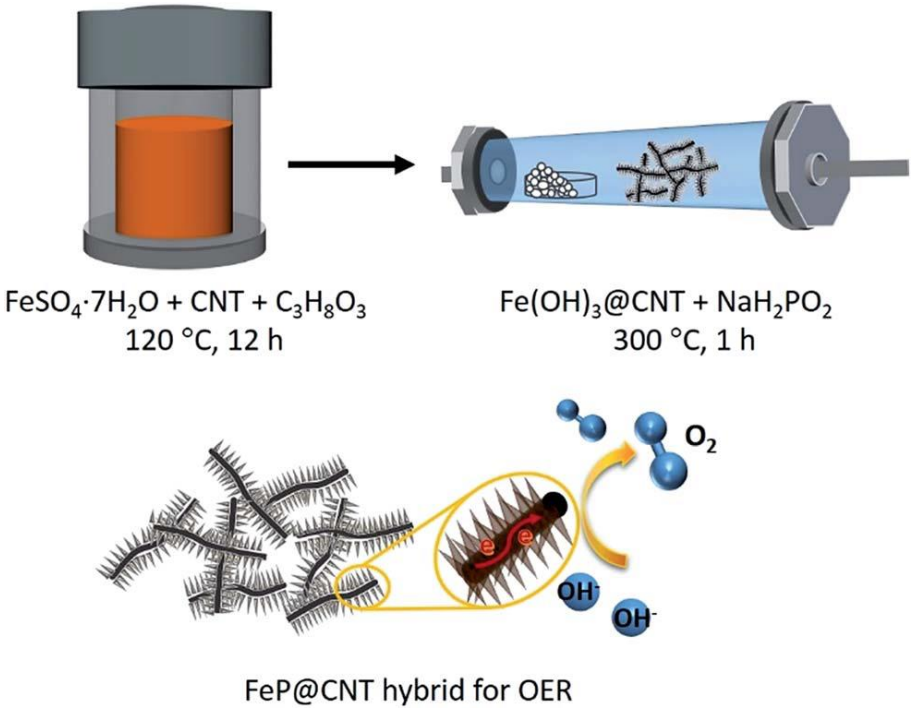


**Figure 2-4.** Schematic illustration of the formation of hierarchical hybrid material for OER catalysis.[30] Reproduced with permission from ref [30]. Copyright 2016, Royal Society of Chemistry.

### Metal nitrides

One-dimensional nanowire array, which grew on the current collector, have been widely invested for OER in the last decade. Most researchers were focusing on the metallic oxide nanowire.[31] However, the OER catalytic performances were significantly limited by the charge transferability between the interfaces of arrays and current collector.[32] Thus, it was desirable to design the array with direct growth on the substrate. According to density functional theory, $Co_4N$ was able to form porous nanowire array and became a preferred platform for OER. Chen and co-workers had fabricated metallic $Co_4N$ nanowire on carbon cloth with good activity and Tafel slope of 44 mV $dec^{-1}$. As a similar design strategy, Zhang et al. converted $Co_3O_4$ nanowires into CoN by using $N_2$ radio frequency plasma at room temperature for a rapid time.[33] The successful transformation was demonstrated by X-ray photoelectron spectra (XPS). The peak corresponding to $O^{2-}$ ions was significantly decreased in O 1s spectra after plasma treatment. In consequence, CoN nanowire array with the preserved porous structure only required an overpotential of 290 mV at 10 mA $cm^{-2}$ and showed a Tafel slope of 70 mV $dec^{-1}$.

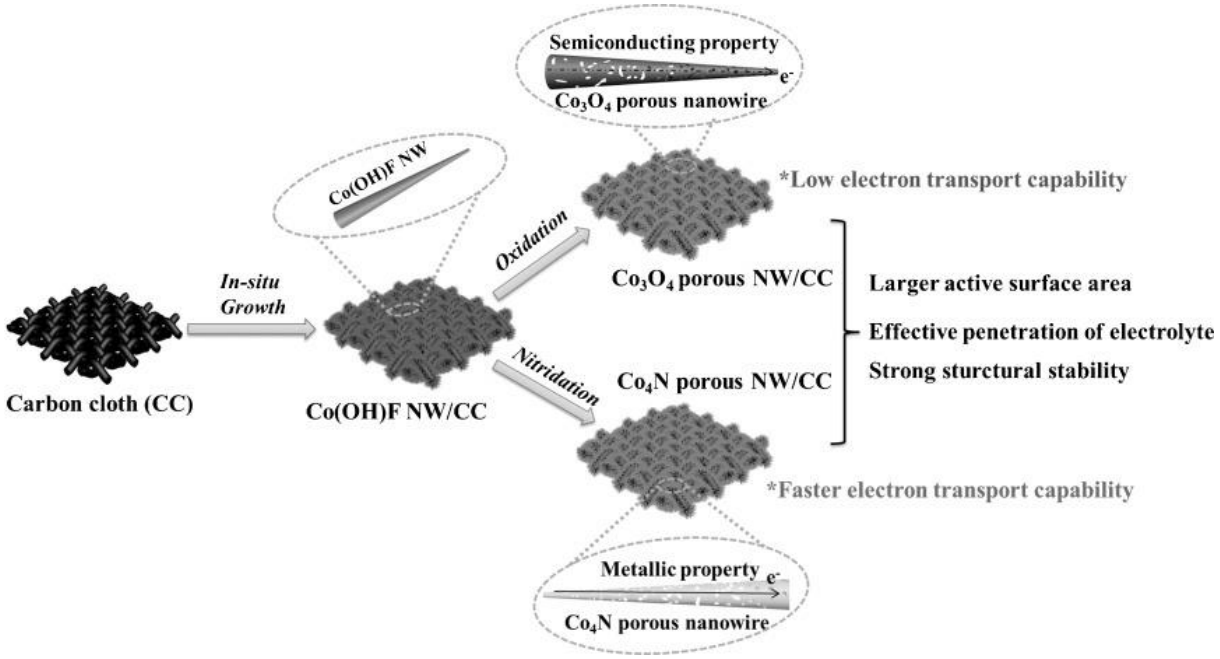


**Figure 2-5.** Schematic illustration of preparation for $Co_4N$ nanowire growing on carbon cloth.[32] Reproduced with permission from ref [32]. Copyright 2015, John Wiley and Sons.

### 2.2.3. Carbon-based materials

Recently, carbon-based materials, such as CNTs and GO, were widely studied for OER application due to their extremely high electrical conductivity. Meanwhile, doping of elements (e.g., N, S, P, and O) and adjusting geometrical morphology were able to make further improvement on their performances. Take activated carbon materials as a typical example, Pi et al. used fallen leaves as the source of carbon and activated it by KOH and $K_2CO_3$.[34] This hierarchical porous carbon had outstanding electro-catalytic activity on OER because of its high surface area (up to 1900 $m^2$ $g^{-1}$). Similarly, porous graphene sheet with the plentiful of active sites successfully grew under argon microwave-induced plasma from graphite oxide.[35]

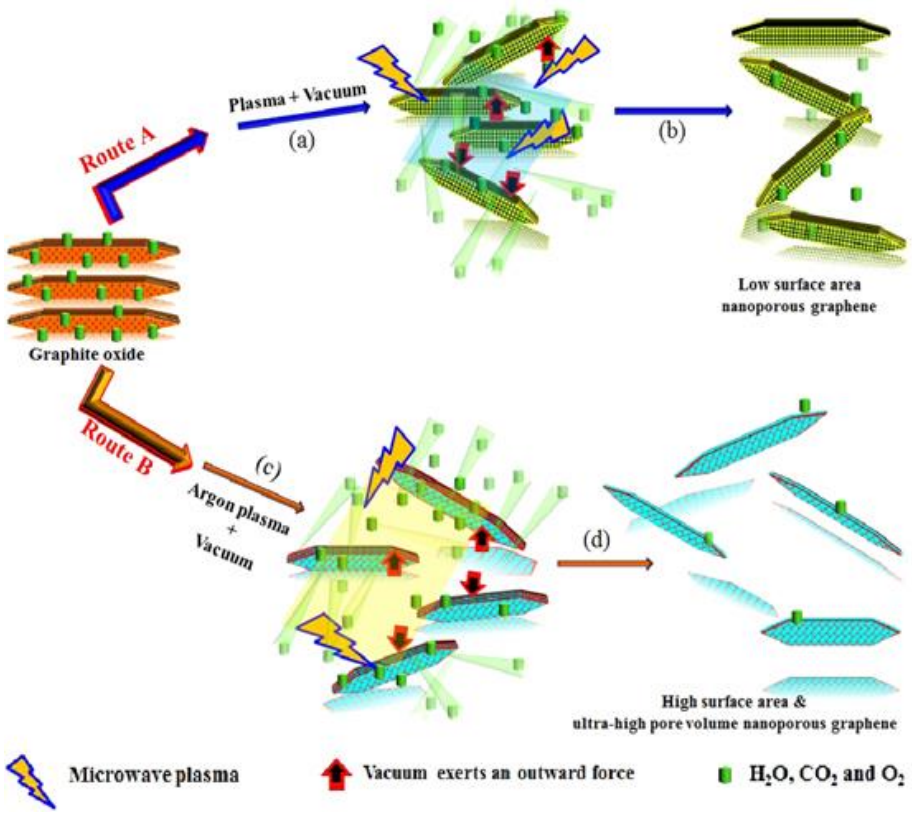


**Figure 2-6.** Schematic illustration of preparation for porous graphene.[35] Reproduced with permission from ref [35]. Copyright 2014, IOP Publishing.

### 2.2.4. Metal-organic frameworks (MOFs)

Typically, there are two kinds of electrocatalysts. Homogeneous catalysts work under molecular scale with high activities. For OER catalysis in alkaline condition, the catalysts are expected to be soluble in order to adequately absorb hydroxyl, but the poor recoverability severely limits their practical applications. In contrast, heterogeneous catalysts are reusable, but the reaction is mainly catalysed at the interface between solid catalyst and liquid electrolyte. The numbers of exposed active sites on the solid surface are generally unsatisfactory. When it comes to MOF, it is a novel kind of porous materials with many outstanding properties. Thanks to their unique structures, MOFs can perform the advantages of both heterogeneous and homogeneous catalysts.[11b] The nano-dimensional porous structures result in atomically dispersed active sites that are able to be efficiently accessed during electro-catalysis. Meanwhile, MOFs are crystalline solids and conveniently recyclable after use. Nohra et al. firstly reported POM-based MOF as electrocatalysts in 2011, which exhibited good performance on HER with the anodic shift of 260 mV.[36] Qin et al. successfully synthesised two POM-based MOFs showing good stability under air and acid conditions. The materials were utilised

as electrocatalysts on HER and exhibited high activities with the Tafel slope of 96 mV $dec^{-1}$.

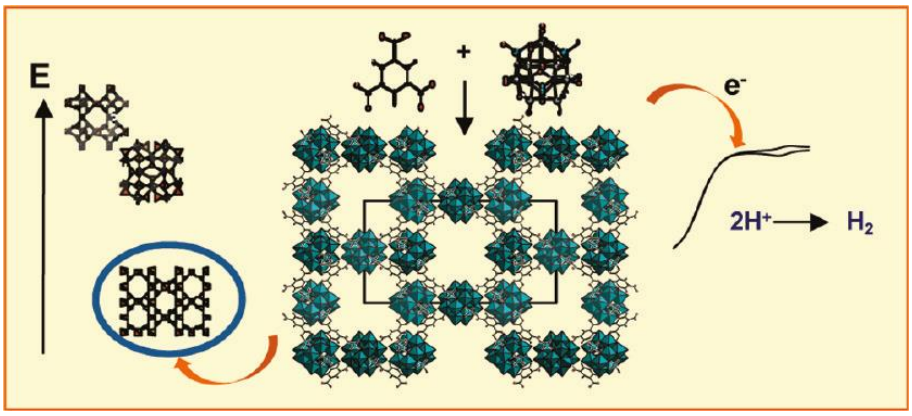


**Figure 2-7.** Polyoxometalate-based metal-organic framework for hydrogen evolution reaction catalysts.[36] Reproduced with permission from ref [36]. Copyright 2011, American Chemical Society.

## 2.3. Overview of MOFs

### 2.3.1. Unique structures and properties

Generally, MOFs were assembled by well-organised metal ions and organic ligands through coordination bonds.[2b] Due to their modifiable morphologies and microstructures, the high specific surface area and a large number of active sites can be achieved by tuning on fabrication methods. The composition of MOFs has the flexibility of adjustment with various ligands or metal centres. Therefore, some earth-abundant metals, such as iron or cobalt, can be utilised instead of precious metals. Moreover, the unique structure of MOFs makes them suitable on the utilisation as templates and fabrication carbon-based nanomaterials.[37] Forming with steady and controllable microstructure, the carbon-based nanomaterials may perform high charge transferability and large specific surface area with atom vacancies. These two changes are expected to result in high catalytic activity.

### 2.3.2. Synthesis routes

Since the first MOF was achieved by a solvothermal method, the outstanding properties of MOFs have attracted increasing attention from scientists.[2a, 38] Therefore, various synthesis routes have been used in the fabrication of MOFs and the following sections show some typical examples.

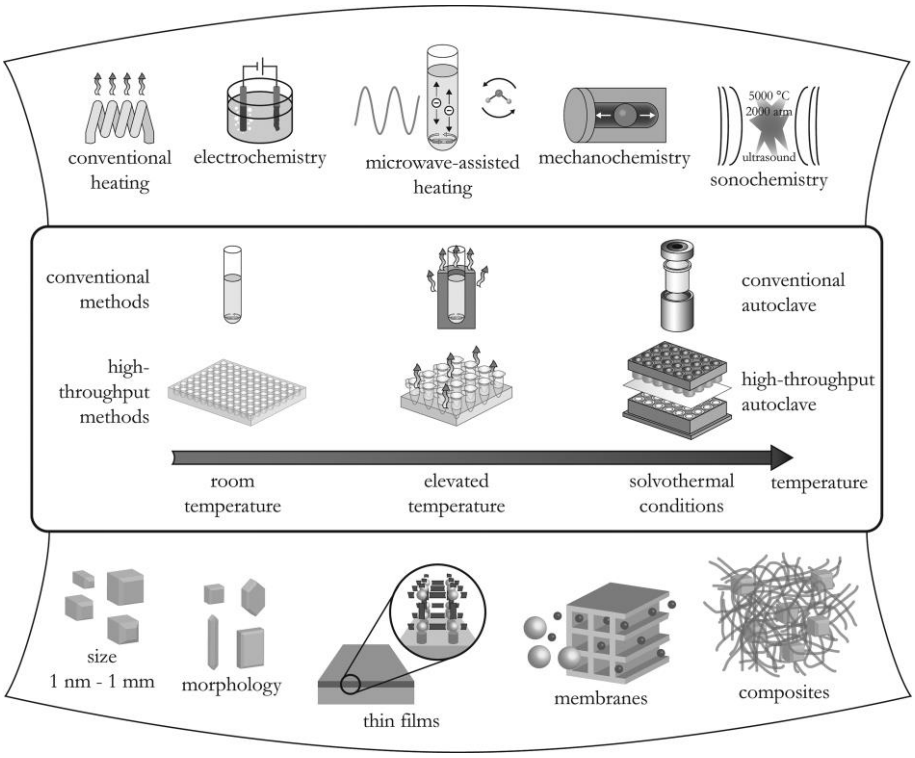


**Figure 2-8.** The overview of MOF synthesis methods, preparation temperatures and potential products.[38] Reproduced

with permission from ref [38]. Copyright 2012, American Chemical Society.

### Conventional method

The conventional method means that the mixed solution of metal-containing precursors and organic ligands are heated to a certain temperature so that other parallel reactions will be avoided. These methods, which require a higher temperature than the boiling point of the solvent at atmosphere, and thus take place in sealed vessels to achieve high pressure, are called solvothermal methods.[39] This kind of method contributes to compounds of some elements in oxidation states. MOF-74 were obtained by the solvothermal method with coordinate unsaturated metal sites (Figure 2-9).[40] The other kind of method is non-solvothermal, indicating that MOFs can be obtained under the temperature lower than the boiling point. For instance, Zeolitic imidazole framework-67 (ZIF-67) is a typical example and fabricated by simply stirring under room temperature.[41] NiCoFe hierarchical foam-like MOF was synthesised in room temperature and the process only took one hour.[42]

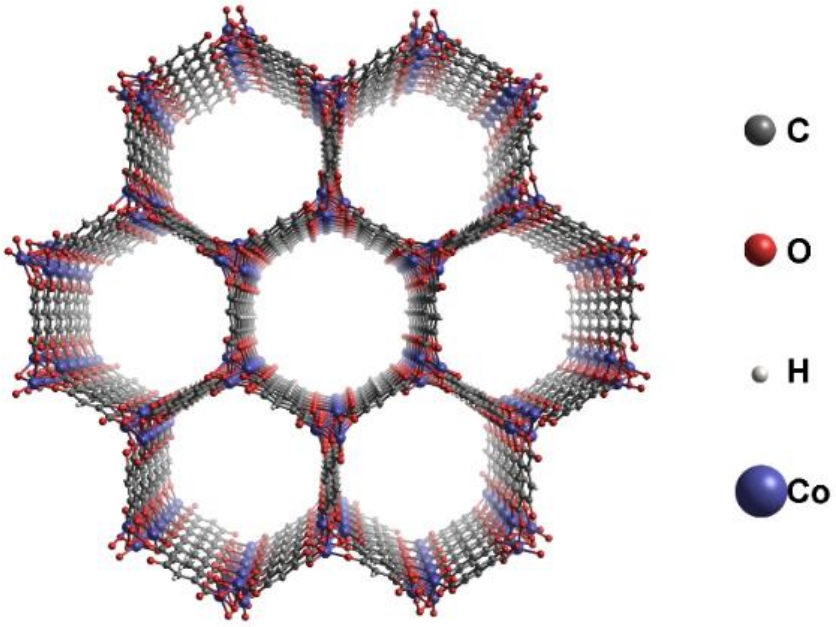


**Figure 2-9.** Analog of Co-MOF-74.

### Microwave-assisted method

Microwave-assisted method is an energy efficient route for MOFs' synthesis.[43] Since it relies on the direct interaction between radiation and reactants, the appropriate starting material and input energy level need to be selected for the rapid and homogeneous heating. The advanced microwave oven

allows the monitor to be presented for precisely control pressure and temperature. For instance, Jhung et al. firstly reported the successful synthesis of MOF (chromium trimesate, MIL-100) with the assistance of microwave.[44] Maik et al. compared different synthetic methods of MOF [$Cu_3(btc)_2(H_2O)_3$] (btc = benzene-1,3,5-tricaboxylate).[45] Among them, microwave-assisted solvothermal synthesis provided the fastest route with promising controllability of product formation.

**Electrochemical method**

Mueller et al. firstly reported the novel and large-scale electrochemical approach of MOF synthetic method.[46] The bulk copper plate was presented as anode in the electrochemical cell. It introduced metal source via dissolving into the solvent, which contained organic linker and conductive salt. The electrochemical method performed a continuous and massive route so that MOF powders could be formed into large industrial geometries.[45, 47] In another comparative research, Rob et al. demonstrated the uniform MOF thin film and patterned coating with the aid of electrochemical synthesis. The method enabled $Cu_3(BTC)_2$ to incorporate as a functional coating on the quartz crystal microbalance.

**Mechanochemical method**

Mechanochemical method, especially grinding process, can produce discrete coordination complexes that contribute to synthetic chemistry and polymer fabrication.[48] Anne et al. firstly reported a solvent-free synthesis method for MOF ($Cu(INA)_2$, INA: isonicotinic acid).[49] Copper acetate and isonicotinic acid were ground by ball-milling rapidly, thereafter, the crystalline and porous products were obtained. This work provided an efficient method on fabricating microporous MOFs with saving the costs of energy, time and material resources.

**Sonochemical method**

The sonochemical method is established based on the assistance of powerful ultrasound with reactants.[50] Ultrasound is the mechanical wave with the frequency between 20 kHz to 10 MHz, which forms the cyclic alternating areas (compression and rarefaction). The cavitation process during ultrasonic approach can rapidly release the accumulated energy; and thus performs high temperature and pressure in the concentrated areas (around 200 nm). Qiu et al. firstly investigated the rapid synthesis of $Zn_3(BTC)_2$ via ultrasonic route.[51] Compared with the conventional solvothermal method

(required 140 °C for 24 h), this work showed a promising approach with convenient conditions. In another research from Jung et al., high-quality MOF-177 was synthesised with uniform crystal size by sonochemical method.[52] This product also exhibited the highest BET surface area among all the samples from various synthetic routes, which might contribute to $CO_2$ absorption capacity.

### 2.4. Strategies for designing MOF-based electrocatalysts

In order to utilise the beneficial properties and move beyond the limitation of MOFs (e.g., poor electronic conductivity), many strategies were developed of deriving MOFs for electro-catalysis.

#### 2.4.1. Low-dimension synthesis

In addition to designing and compounding new MOFs with partially coordinated metal centres, synthesizing nano-sized MOFs and low dimensional MOFs (e.g. 2D MOF nanosheets) can effectively enrich CUMSs. Moreover, the highly accessible surface also facilitates the creation of CUMSs through solvent extraction. For example, Zhao et al reported ultrathin NiCo MOF nanosheets based on the ultra-sonication during synthesis to catalyse OER.[11b] The coordination bonds between benzenedicarboxylic acid (BDC) and metal centres were partially terminated so that the CUMSs were exposed on the surface. As a result, the NiCo-MOF nanosheets showed an overpotential of 250 mV to reach the current density of 10 mA $cm^{-2}$ in 1 $_M$ KOH solution, which is much lower than that of the bulk NiCo-MOF (317 mV). In the same way, Hai and co-workers developed NiFe bimetallic MOFs nanosheets and applied as catalyst for OER in alkaline solution.[53] The MOFs nanosheets performed a low overpotential of 260mV at current density of 10 mA $cm^{-2}$. They purposed the great performance owing to abundant CUMSs on the material surface.

Duan et al synthesised MOF nanosheet array via in-situ growth on the substrate and the catalyst showed a small overpotential of 240 mV at 10 mA $cm^{-2}$ (Figure 2-10).[54] Therefore, the 2D engineering of MOFs has been widely studied and applied (e.g. cobalt dithiolene integration,[16] growth direction restriction[55] and $Hf^{4+}$ cluster capping[56]). However, even though these methods are efficient on synthesizing 2D MOFs, the modulator (e.g. surfactants) using in the synthesis may block the active sites of catalysts that reduce their catalytic activities.

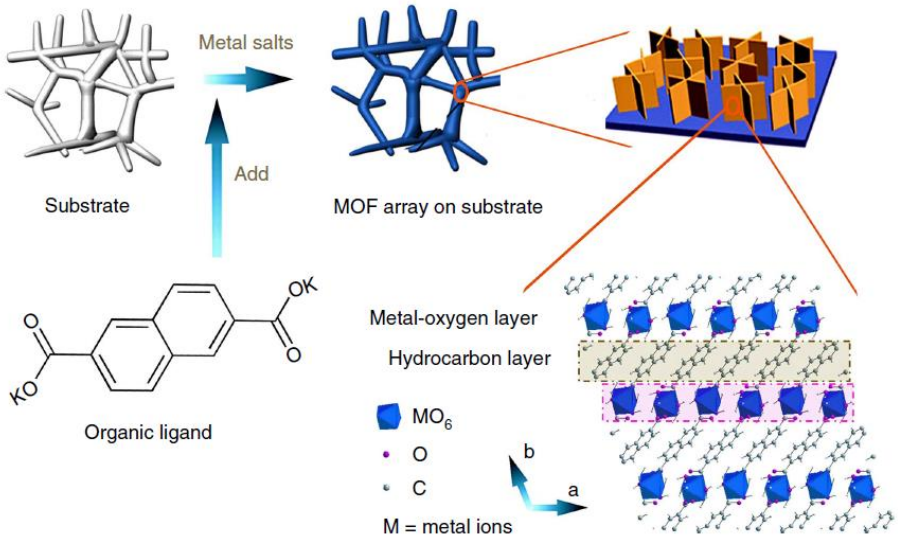


**Figure 2-10.** Synthetic process of MOF nanosheet array.[54] Reproduced with permission from ref [54]. Copyright 2017, Nature Publishing Group.

As an alternative strategy, some MOFs with weak interaction between layers (such as van der Waals forces) are able to be exfoliated into nanosheets.[10, 55, 57] The exfoliated MOF nanosheets might exhibit large surface area and expose extra active metal centres for enhanced electro-catalytic activity. Meiting et al. synthesised Zn-TCPP (TCPP means tetrakis, 4-carboxyphenyl, porphyrin) ultrathin nanosheets with the aid of surfactants.[55] Compared with bulk Zn-TCPP MOF synthesised by the conventional method, the BET surface area of anisotropic nanosheets was significantly increased to 391 $m^2 g^{-1}$ and was almost two times higher than the surface area of conventional MOF.

Yuan et al. successfully prepared 1-nm-thick molecular sieve nanosheets via the exfoliation from layer MOF precursor.[58] As shown in Figure 2-11, each metal atom was coordinated by four ligands in distorted tetrahedral geometry that formed two-dimensional layers connected by van der Waals interactions. In order to avoid latent structural damage, they wet ball-milled the precursor at low speed (60 rpm), so that the solvent molecules would easily penetrate into layered MOF. Thereafter, the material was exfoliated with the help of ultra-sonication and exhibited superior performance as membrane.

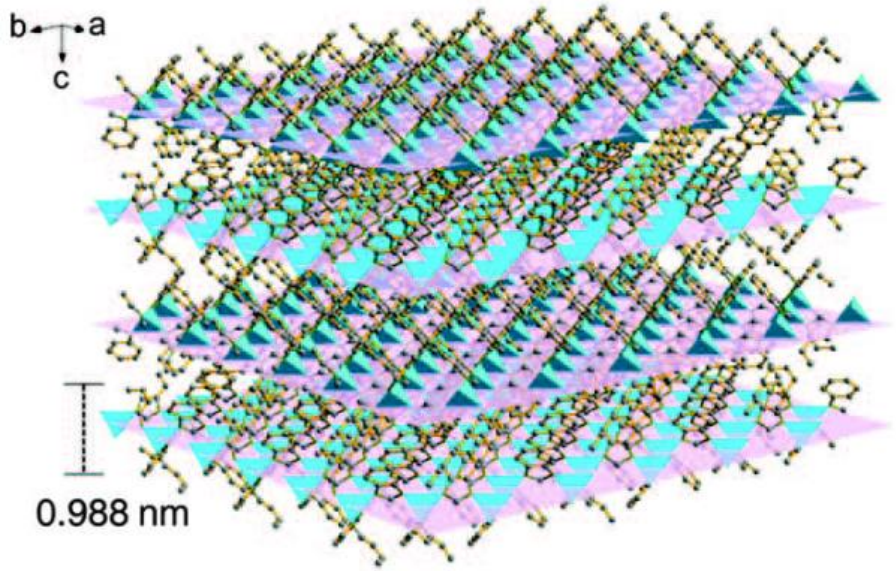


**Figure 2-11.** Analog of MOF precursor. The purple planes were highlighted to illustrate layered structure.[58] Reproduced with permission from ref [58]. Copyright 2014, The American Association for the Advancement of Science.

### 2.4.2. Morphology control

Fine-tuning morphology of MOFs was widely utilised for the purpose of exposing extra active sites and improving surface adsorption capability that played a critical role in the development of electro-catalysis.[1, 59] Qizhu et al. presented the preparation of hierarchical trimetallic NiCoFe-based MOF nanostructure via a simple and scalable method at room temperature (Figure 2-12).[42] Three metal acetates were performed as metal sources with the optimised atomic ratio of Ni/Co/Fe to synthesise hierarchical foam-like morphology, which provided an appropriate platform for active components exposure. Consequently, the ultimate catalyst showed outstanding activity for OER (with the overpotential of 257 mV to reach the current density of 10 mA $cm^{-2}$), which was contributed to favourable charge transferability and the exposing of extra active sites.

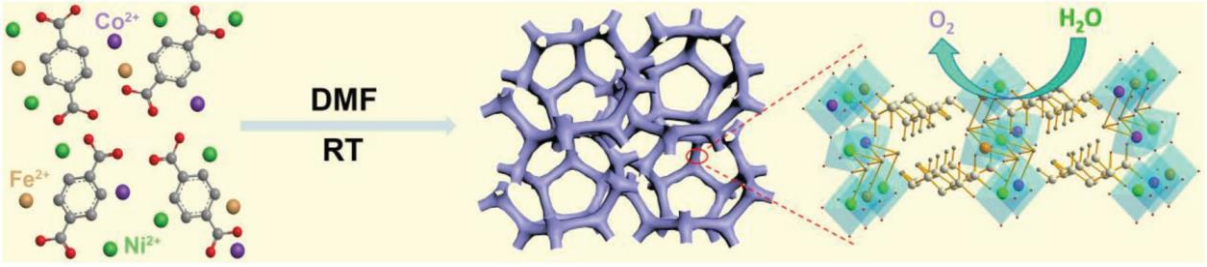


**Figure 2-12.** Illustration of the formation process of hierarchical trimetallic NiCoFe-based MOF nano-foam.[42] Reproduced with permission from ref [42]. Copyright 2019, John Wiley and Sons.

In another study, Lei et al. reported the synthesis of MOF-derived nano-cages tailored by a facile chemical etching at room temperature.[60] The as-synthesised MOF was transformed into an unusual structure with pyramid-like walls, sharp edges and similar size (Figure 2-13), which might be contributed by the inhomogeneous surface reactivity of the cubes. Due to the hollow structure and high surface-area-to-volume ratio, the NiCo mixed oxides nano-cages manifested improved electro-catalytic activity for OER (with the overpotential of 380 mV at current density of 10 mA $cm^{-2}$).

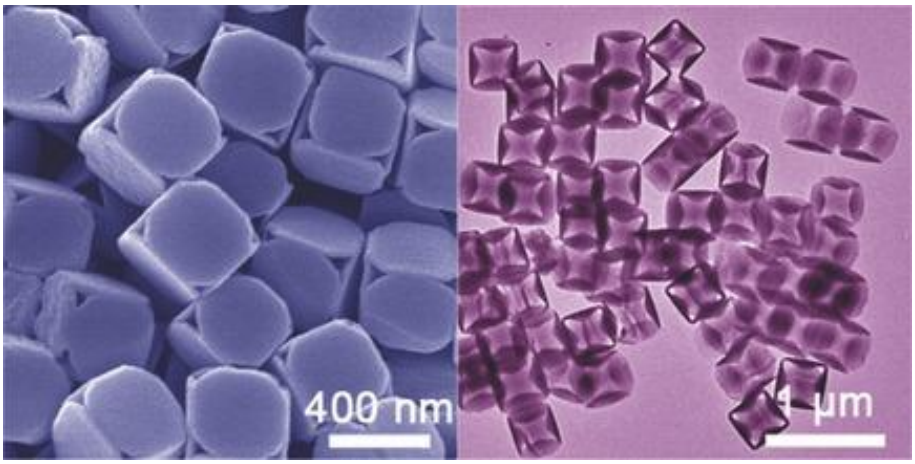


**Figure 2-13.** SEM (left) and TEM (right) image of the NiCo nano-cages with average size of 400 nm.[60] Reproduced with permission from ref [60]. Copyright 2016, John Wiley and Sons.

### 2.4.3. Hybridisation composites

Graphene is the one-atom-thick carbon sheet which can be considered as the single layer of graphite.[5c] Most of the graphene products are fabricated by oxidation and exfoliation of graphite. Ultimately, the product with single or few layers is known as graphene oxide (GO).[61] As we know, the carbon atom has four electrons in its outer shell. Thanks to the hexagonal lattice of graphene, each atom connects to other three atoms to form two-dimension layer by electron pairs. Hence, there is one electron freely in the third dimension which is expected to show high electronic conductivity and contribute to electro-catalytic activity.[62]

The important role to achieve composites is the epoxy groups on GO surface, which were introduced through the oxidising process, and the mechanism has been analysed by Camille et al..[5c] Figure 2-14 shows the formation steps of MOF-5/GO composites, where the small unit of MOF-5 attaches to the few layers of graphite oxide. The reason for the good connection is that the epoxy groups could

replace the oxygen atoms in MOF. They took the same function as the oxygen atoms of water (inducing decomposition of MOF-5 in water) and was analysed by Greathouse and Allendorf.[5b] The porous structure of MOF could be maintained due to the limited number and restricted spatial location of epoxy groups. In addition, the oxidation procedure transformed graphite into GO and introduced defects in the graphene layers.[5c] This alteration enhanced the hydrophilicity of GO and enabled its good dispersion in the water. Therefore, it could achieve good diffusion during the synthesis of MOFs and form composites with a homogeneous structure.

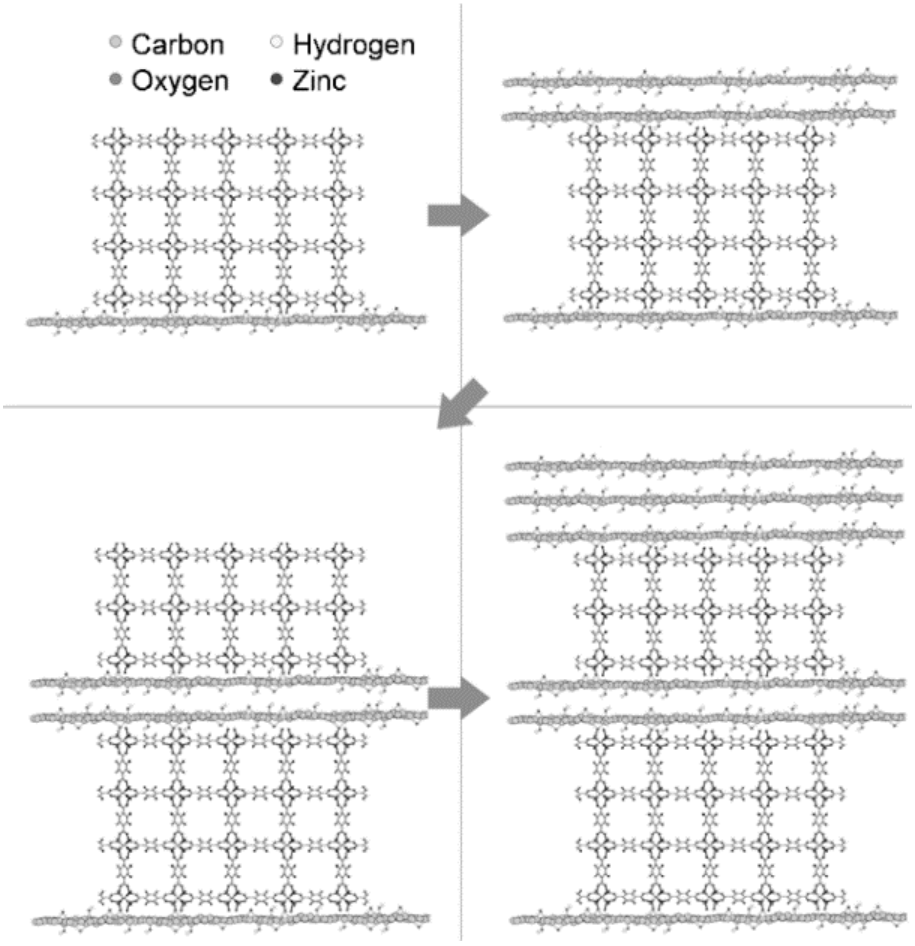


**Figure 2-14.** Synthesis scheme of the step 1 to 4 for MOF-5/GO composites.[5c] Reproduced with permission from ref [5c]. Copyright 2009, John Wiley and Sons.

Maryam designed GO/copper-based MOF hybrid composite, in which the structure could coordinate with two strong electronegative ligands and enhance its stability in an acid environment.[63] As a result, the composite with 8 wt% GO exhibited improved OER activity with the lower onset potential (1.19 V) vs. reversible hydrogen electrode (RHE) in 0.5 M $H_2SO_4$ solution. The catalyst also showed great electro-catalytic activity and stability in ORR, HER and polymer electrolyte membrane fuel cell

testing due to the incorporation of GO in MOF. Moreover, in order to obtain uniform and dense ZIF-8 particles on GO surface, Zhong et al. added polyvinylpyrrolidone (PVP) as modulator prior to the formation of MOFs.[64] PVP might enrich the functional groups and coordinate metal ions to achieve uniform nucleation of ZIF-8 on GO surface. Thus, they successfully synthesised dispersive two-dimension ZIF-8/GO composite, which could be carbonised into graphene-based nitrogen-doped porous carbon sheets. The ultimate material achieves a consecutive conductive network and showed good activity as a promising catalyst for ORR that was contributed to the synergistic effect of nitrogen-doped carbon sheets and graphene.


**Figure 2-15.** Illustration of the fabrication procedure for ZIF-8/GO composite.[64] Reproduced with permission from ref [64]. Copyright 2014, John Wiley and Sons.

Yan et al. previously implanted Ni-MOF-74 on GO substrate to generate nanocrystals, followed by calcination with sodium hypophosphite.[62b] Its uniform growth was considered as the contribution of coordination effect between Ni cation and oxygen species on GO. The method is able to enhance material charge transfer efficiency for the superior activity on both HER and OER. However, the crystalline and unique porosity of former composite was not retained from pristine MOF, which shows the demand for research to further tune its microstructure.

### 2.4.4. Conventional pyrolysis

In order to achieve enhancement, MOFs were expected to provide specific elements sources or the

periodic arrangement of metal centres with porous structure.[9, 64-65] Generally, they were placed in a furnace as precursors and heated (600 ~ 1000 °C) for several hours under argon or nitrogen protection atmosphere. For example, Dengrong et al. reported the fabrication of carbon-coated CoNi alloy nanoparticles embedded in carbon matrix (Figure 2-16).[66] The material was synthesised from CoNi-MOF-74 via a facile calcination process and showed good performance toward OER (with the Tafel slope of 126 mV $dec^{-1}$ in 0.1 $_M$ KOH) due to the high charge transferability of carbon shell.

In addition, Bao et al. directly synthesised N-doped carbon nanotube frameworks that were derived from ZIF-67 via pyrolysis process.[9] During this work, ZIF-67 not only served as the source of C and N elements, but also performed as a template for the unique morphology. The hollow-structured hierarchical carbon nanotube frameworks were formed through the pyrolysis under $Ar/H_2$ atmosphere, followed by acid leaching. As a result, the MOF-derived functional material exhibited enhanced activities for ORR and OER (with the Tafel slope of 93 mV $dec^{-1}$ in 1 $_M$ KOH), that might be due to the carbonisation of catalysts. Furthermore, Kaifeng et al. interred Co-MOF-74 at 800 °C under nitrogen protection.[67] The carbonised Co-C material exhibited a core-shell porous structure and showed enhanced absorption performance toward microwave.

The electrochemical properties (e.g., charge transferability) were improved after pyrolysis processes; however, it was still challenging to maintain the unique structure of MOFs under these high temperatures even though they were heated up with relatively low rates (1 ~ 3 °C $min^{-1}$). In other words, the atomically dispersed metal centres easily formed agglomerates or be wrapped by other components that could not sufficiently expose active sites.

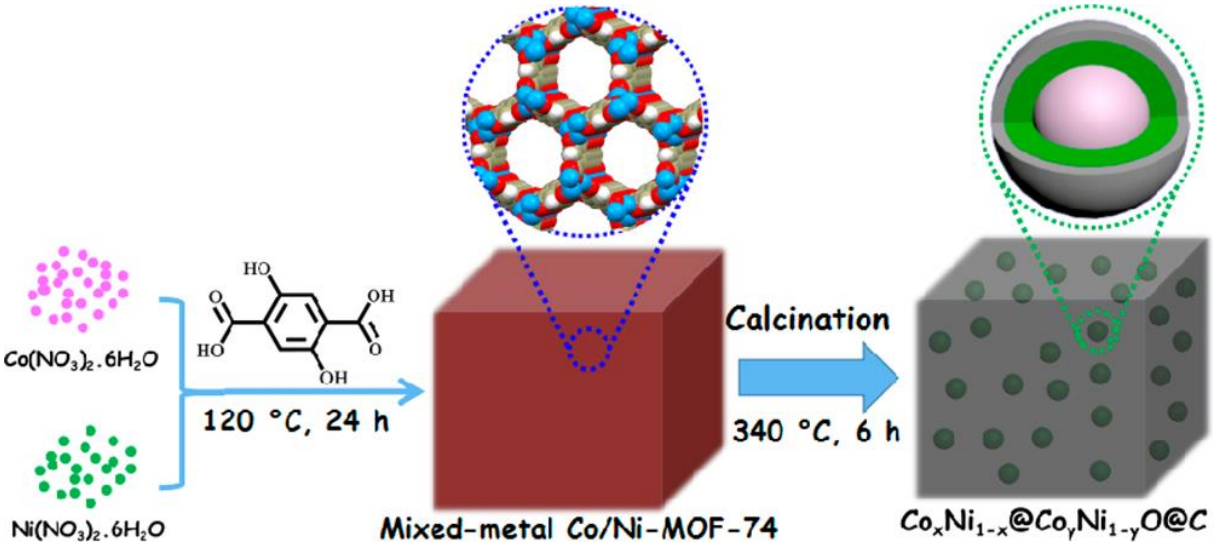


**Figure 2-16.** Illustration of the synthetic scheme for carbon-coated CoNi alloy nanoparticles embedded in carbon matrix.[66] Reproduced with permission from ref [66]. Copyright 2017, American Chemical Society.

### 2.4.5. Plasma engraving

The pyrolysis of metal-oxides and MOFs by furnaces had been reported before.[68] These precursors had been placed into the high-temperature furnace with inert gases protection. Even though the electrocatalysts could be obtained by direct carbonisation with enhanced charge transferability, the porous structures were hardly maintained. As a result, the surface area would be seriously decreased and most of the active sites were stopped from exposing. Comparing with this conventional method, plasma treatment is a novel method that could improve many properties of MOFs without serious influences on their structures.

As we know, there are four fundamental states of matter in the world, which are solid, liquid, gas and plasma. Comparing with the other three states, plasma has unique properties and hardly exists in nature. Generally, plasma can be generated by applying gases in high temperature or strong electromagnetic field. These conditions can achieve the point where atoms are ionised to positive and negative ions.[69] Due to a large number of charge carriers, plasma has high electric conductivity and sensitivity to the electromagnetic field. Thus, it can be easily controlled and shaped by a magnetic field.

In recent years, plasma has been applied to many chemical reactions and materials according to its eco-friendly and energy-saving characters.[35] In this research, plasma treatment can be considered as

rapid and controllable operation with especially high efficiency on the materials. Plasma with the appropriate intensity and duration will not collapse the structures of porous materials but even introduce defects to improve their characters. For example, some MOFs have poor stability toward the water, but researches showed that a plasma-treated material can prevent itself from the decomposition by water. Jared B. Decoste et al. studied on a modification method for Cu-BTC, that is plasma-enhanced chemical vapor deposition of perfluorohexane (PFH).[70] After plasma treatment, the Cu-BTC maintained its smooth surface without cracks under 90% humidity, because the PFH located in large pores could restrain the formation of water clusters.

The mass transferability of material can be improved by large and abundant pores. In this aspect, plasma is able to etch MOFs to enlarge the apertures of pore and optimise pore volume. Jared B. Decoste used to modify Zr-based MOFs by plasma in order to develop hierarchical pore structures.[71] As a consequence, the UiO-66 series of MOFs were etched by plasma with perfluoroalkanes and showed enhanced mass transferability toward detoxification reaction.

Regarding OER, the catalysis merely takes place on the external surface of bulk MOFs. Therefore, the incorporation of missing linker and missing node defects by plasma engraving has the potential to be less time-consuming and more cost-effective than other processes.[72] Li and co-workers enriched CUMSs on a fully coordinated MOF (ZIF-67) through dielectric barrier discharge (DBD) plasma treatment.[14] It partially removed organic ligands from metal centres of MOFs and generated mono-dispersed CUMSs (Figure 2-17). Due to the remained porous structure and exposed metal atoms, the CUMSs-enriched catalyst showed a much lower overpotential (320 mV) at 10 mA $cm^{-2}$ than pristine ZIF-67 (400 mV) in $O_2$ saturated 1 $_M$ KOH aqueous solution. Moreover, the turnover frequency (TOF) of CUMSs-enriched ZI-67 (0.462 $s^{-1}$ at the overpotential of 300 mV) was also improved from pristine ZIF-67 (0.043 $s^{-1}$). Nevertheless, compared with other MOFs, the OER activity of plasma treated ZIF-67 was still limited by the instinct coordination structure. The extensive and fine control of this technology raises the flag for the need of investigations on further optimising CUMSs. In another work from the same group, argon plasma was used on engraving $Co_3O_4$ nanosheets.[73] Higher surface area and more oxygen vacancies were brought by this rapid treatment than pristine material. Both of them could lead to high electro-catalytic activity; therefore plasma-engraved nanosheets presented higher current density at 1.6V vs. RHE and lower onset potential than

pristine $Co_3O_4$ nanosheets.

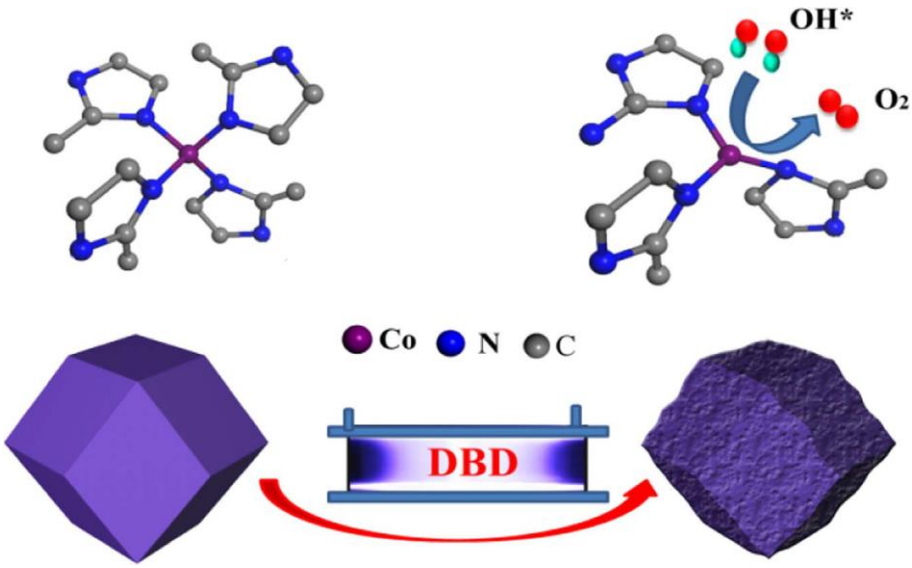


**Figure 2-17.** Illustration of the preparation of CUMSs enriched ZIF-67.[14] Reproduced with permission from ref [14]. Copyright 2017, Elsevier.

## 2.5. Conclusion

The energy requirement is persistently growing that leads to the tremendous attention of hydrogen energy development. The high demand and widespread consumption of hydrogen energy raises the flag of the independence from fossil fuel as well as green gases emission. In this aspect, water splitting is one of the effective and sustainable routes for hydrogen production. As a crucial half-reaction of water splitting, OER highly needs to be catalysed, which is mainly due to its sluggish kinetics, for economical and sustainable hydrogen production. Therefore, the efficient catalysts are highly desired for reducing the onset potential of OER.

Generally, noble-metal based catalysts (e.g., Ru, Pd and Ir) were used to save the costs of energy and money. They performed good activity and stability for OER under alkaline and acid environment. $RuO_2$ and $IrO_2$ were also considered as the standard criteria for other catalysts. However, the rare accessible resources and high costs limited their application on the large-scale industry. In the view of rarity, earth abundant-metal based materials played the alternative role of electrocatalysts. Metal oxides, metal phosphides and metal nitrides were widely investigated due to their inexpensive costs and preferable efficient for OER. In addition, carbon-based catalysts, such as carbon nanotubes and porous carbon sheets, exhibited notable electronic conductivity as a good substrate of catalysts. Nevertheless, since metal centres are regarded as the active sites of OER, these catalysts are expected to be further studied on electro-catalysis.

Above all, MOFs have the potential to be developed as electro-catalysts in order to overcome the high activation energy of OER. Their outstanding properties (e.g. high surface area, atomically dispersed metal centres and tuneable microstructure) allow active sites to be exposed and utilised for excellent performance on electro-catalysis. Thus, these catalysts are able to achieve better activities (with overpotential less than 300 mV at current density of 10 mA $cm^{-2}$) than noble metal-based electrocatalysts.

However, there are still some challenges in further improving MOFs' characteristics. The relative low electrical conductivity, stability, absorption ability toward reaction media and the number of exposed active sites still limit the further improvement of their activities. Based on that, Table 2-1 summarises typical strategies for designing MOF-derived materials as electrocatalysts in previous reports. These

methods might introduce functional ions, expose extra active sites or increase electronic conductivity, which were expected to improve electro-catalytic performance for catalysts.

**Table 2-1. Summarised** strategies for designing MOF-based electrocatalysts

| Strategy | Examples | Benefit | Limitation |
|---|---|---|---|
| Low-dimension synthesis | NiCo-BDC nanosheets,[11b] NiFe 2D array.[54] | Highly accessible surface and enriched CUMSs. | Structural deterioration and morphological damage might hamper MOF from achieving good activity. |
| Morphology control | Hierarchical NiCoFe nano-foam,[42] NiCo nano-cages.[60] | Some used one-pot scalable method, which enhanced the surface absorption capability to the reactants. | Latent blocking of active sites by modulator. |
| Hybridisation composites | MOF-5/GO composites,[5c] ZIF-8/GO composites.[64] | The charge transferability and surface area might be improved for electro-catalysis. | The incorporation and nucleation progresses needed to be optimised for homogeneous catalysts. |
| Conventional pyrolysis | Carbon-coated CoNi nanoparticles embedded in carbon matrix,[66] N-doped carbon nanotube framework.[9] | Highly electronic conductivity with porous structure. | The atomically dispersed metal centres of MOF were easily agglomerated or wrapped, that could not be sufficiently exposed to reactants. |
| Plasma engraving | Plasma etched UiO-66,[71] CUMSs enriched ZIF-67.[14] | Etched MOF for exposing CUMSs or enhancing mass transferability with abundant pores. | The effects of plasma conditions (species, duration and intensity) needed to be further studied since its mechanism was still unclear. The treatment should be investigated to focus on the catalysts surface where OER mainly take place on without the damage of MOF porous structure. |

This project aims to develop the design strategies of MOF-derived catalysts in order to move beyond the shortcoming of MOFs (e.g., poor conductivity, insufficient CUMSs exposure), at the same time, the electro-catalytic performance can benefit from their outstanding properties (e.g., atomically

dispersed metal centres, porous structure). In the first study, plasma engraving was applied on Co-MOF-74 to introduce structural defects and expose extra CUMSs. The effects of plasma conditions were investigated that proved the relation of CUMSs and electro-catalytic performance. In the second study, the charge transferability of Co-MOF-74 was significantly enhanced with the aid of GO intercalation that contributed to the improvement of its activity toward OER. The details of the research approaches are shown in the following section.

# Chapter 3. Research Method

The pristine Co-MOF-74 is named as "**MOF**" through the following sections. In the first study (plasma engraving), the MOFs engraved by argon and hydrogen plasma at an optimal treatment duration of 13 min and a power of 100 W are named as "**MOF-Ar**" and "**MOF-$H_2$**", respectively. The samples engraved with specific durations or power other than the optimal conditions have been added a suffix, for example, "MOF-Ar-15 min" indicates a pristine MOF engraved by argon plasma at 15 min and optimal power.

In the second study, the samples intercalated with GO are named as "**MOF-X**", where "X" indicates the specific weight percent of GO participating in the synthesis.

### 3.1. Materials and synthesis routes

*Materials:* All chemicals, including Cobalt(II) nitrate hexahydrate ($Co(NO_3)_2 \cdot 6H_2O$, 99%), 2-5-dihydroxyterephthalic acid ($H_4$dobdc, 98%) and N,N-dimethylformamide (DMF, 99.5%) were purchased from Sigma-Aldrich without further purification. GO was purchased from Nanjing JI Cang Nano Technology Co. Ltd. AR grade ethanol and methanol were bought from Merck.

*Synthesis of Co-MOF-74:* $Co(NO_3)_2 \cdot 6H_2O$ (2.377 g) was dissolved in a mixed solution containing distilled water (65 ml), ethanol (65 ml) and DMF (65 ml). Then, $H_4$dobdc (0.482 g) was added during continuous stirring. The as-obtained solution was transferred into a 500 mL Teflon-lined stainless steel autoclave, and then heated in an oven at 100 °C for 24 hours. After cooling down to room temperature, brown power was obtained and collected by centrifugation. The product was washed by methanol with sonication for four times, thereafter, dried in the vacuum oven at 80 °C for 24 hours.

*Synthesis of Co-MOF-74/GO composite:* The preparation process was same as that of Co-MOF-74, except that the specific amount of GO (calculated by the weight percent of dried product) was dispersed in the mixed solution before $Co(NO_3)_2 \cdot 6H_2O$ by ultra-sonication.

### 3.2. Plasma treatment

The microwave-induced plasma came from a SAIREM microwave reactor with the reaction chamber and transparent walls for the microwave.[74] This generator could output power of microwave consecutively from 0 to 2000 W at a frequency of 2.45 GHz. Plasma was generated by microwave reaction in conjunction with a vacuum system, and the pressure was typically ~$10^{-2}$ Torr maintained by a vacuum pump. To treat MOFs under plasma, firstly, MOF sample (30 mg) was loaded into microwave plasma system under protection gas (e.g., argon). Secondly, the reactor chamber was pumped down under purposed carrier gas until a stable pressure within working range was attained and continued for 15 minutes so that impurities were evacuated and the specific atmosphere was formed. Finally, the microwave power was increased to the desired value and the sample was moved to plasma zone for the purposed duration.

### 3.3. Electrochemical measurement

For the first study (plasma engraving), in order to prepare a thin film electrode, a catalytic sample (5.0 mg) and carbon black (5.0 mg, Super P® Conductive, from Alfa Aesar) were sonicated with a mixture of ethanol (0.5 ml) and 5 wt% Nafion solution (50 µl) for 40 minutes.[27a] Then, 5 µl of this suspension were drop-casted and dried on a glassy carbon disk electrode (diameter 0.4 cm with the area of 0.126 $cm^2$). The electrode was polished by PK-3 electrode polishing kit (from ALS Co. Ltd) and cleaned by sonication in ethanol every time before use. The electrochemical measurements were performed in three-electrode cell configuration (Biologic VMP2/Z multichannel potentiostat). The Pt wire and calibrated Ag|AgCl (KCl) were used as counter electrode and reference electrode respectively. The electrolyte was $O_2$-saturated 0.1 $_M$ KOH aqueous solution through bubbling with $O_2$ (99.99% purity) for the entire testing duration. The linear sweep voltammetry (LSV) was used to obtain polarisation curves at a scan rate of 10 mV $s^{-1}$ on rotating disk electrode (RDE).

During the second study (GO intercalation), the measurement procedures are the same as above, except that carbon black was removed from the recipe in order to avoid the synergistic effect between porous carbon and graphene.

All the potentials in this research were compensated with *iR*:

**Equation 5.** *iR* compensated calculation.

$$E_{iR-corrected} = E_{Ag|AgCl} + E_{PH} - iR_u$$

where $E_{PH}$ (0.973 V) is obtained by the calibration of reference electrode (Ag|AgCl, KCL sat.) in aqueous electrolyte (PH = 13). *i* is the current and $R_u$ (55 Ω) is the uncompensated ohmic resistance of electrolyte (PH = 13) between the tip of reference electrode and the surface of working electrode.

The current density (*j*) was derived from:

**Equation 6.** Current density calculation.

$$j = \frac{i}{A_{geo}}$$

where $A_{geo}$ (0.1256 $cm^2$) is the geometric area of the glassy carbon on working electrode.

During the calculation of TOF, the active sites for Co-MOF-74 and plasma etched MOFs in this

research are assumed as the cobalt atoms. The moles of cobalt atoms were estimated through the molecular formula of MOF.[75]

### 3.4. Materials characterisations

To determine the crystal structures of MOFs catalysts, a Bruker D8-Advanced X-ray diffractometer was utilised for X-ray diffraction (XRD) patterns (2θ was from 5° to 50°) with a nickel-filtered Cu-Kα radiation and the scan rate is 0.1° $step^{-1}$.[27a]

The Scanning electron microscope (SEM) images were obtained from JEOL JSM-7001F and Hitachi SU3500 microscopes with the acceleration voltage of 5 kV.

The Transmission electron microscope (TEM) images were performed by Philips Tecnai F20 FEG-S/TEM operating at 200 kV.

Fourier-transform infrared spectroscopy (FTIR) were taken by PerkinElmer Spectrum 100 FT-IR Spectrometer.

As Brunauer–Emmett–Teller (BET) surface area, pore volume and distribution were desired to analyse, nitrogen adsorption measurements were performed at 77 K (boiling point of liquid nitrogen) on a Micromeritics TriStar II 3020 system.[76] The single point adsorption total pore volume ($V_{tot}$) was estimated at relative pressure ($P/P_0$) of 0.99. The micropore volume ($V_{micro}$) and mesopore volume ($V_{meso}$) were calculated using t-plot and Barrett Joyner Halenda (BJH) methods separately.[77]

X-ray photoelectron spectra (XPS) were obtained from a Kratos Axis Ultra spectrometer incorporating with 165 mm hemispherical electron energy analyser and a monochromatic Al Kα (1486.6 eV) radiation source at 150 W (15 kV, 10 mA). All the XPS spectra tuning by the binding energy of C 1s line at 284.6 eV from adventitious carbon as a reference.

Co K-edge X-ray absorption spectra (XAS) were recorded on the multipole wiggler XAS beam-line 12 ID at the Australian Synchrotron, in operational mode 1. The beam energy was 3.0 GeV and the maximum beam current was 400 mA.

Room temperature PL spectra were obtained by using an inVia Raman Microscopy with a He-Cd ultraviolet laser.

# Chapter 4. Fine-tuning the Coordinatively Unsaturated Metal Sites of MOF by Plasma Engraving for Enhanced Electro-catalytic Activity

## 4.1. Introduction

As shown in section 2.3.1, MOFs are a novel class of porous materials that have attracted growing attention in recent years.[1] Generally, they are formed by well-organised coordinate covalent bonds between metal ions and organic ligands, providing atomically dispersed metal centres and accessible active sites for a variety of potential catalytic reactions. These structural characteristics allow MOFs to present the advantages of both heterogeneous and homogeneous catalysts.[11b] Therefore, MOFs have been widely investigated as electrocatalysts for oxygen evolution reaction (OER), hydrogen evolution reaction (HER), oxygen reduction reaction (ORR) and carbon dioxide reduction.[9] Due to their modifiable morphologies and microstructures, the high specific surface area and enriched active sites of MOFs can be obtained by tuning fabrication methods or post-synthetic modifications so as to attain their promising electro-catalysis activities.[1, 78] Therefore, some MOFs based on earth-abundant metals (e.g., iron, cobalt, nickel) can be used to replace precious metals (e.g., ruthenium, iridium) as electrocatalysts for OER.[1, 9, 11c, 79]

As mentioned in section 2.1.3, the atomically dispersed metal centres of MOFs are recognised as potential active sites for the OER catalysis.[1, 11] However, the full coordination of the metal centres usually limits their direct applications as electrocatalysts.[11b, 12] Therefore, abundant active sites can be utilised by reactants without damaging the phase integrity of MOFs via the fine tuning of CUMSs, so that the OER electro-catalytic performance of MOFs can be remarkably enhanced. In this regard, the bottom-up and top-down methods have been applied in order to prepare more CUMSs on MOFs. Namely, the former means the design of a framework structure by tuning the synthesis recipe (e.g., metal salts, organic ligands, solvents or preparation routes), while the latter involves post-treatment methods (e.g., incorporation defects) on synthesised MOFs.

Regarding bottom-up methods, in addition to designing and compounding new MOFs with partially coordinated metal centres, synthesising nano-sized MOFs and low dimensional MOFs (e.g., 2D MOF nanosheets[11b, 54]) can effectively enrich CUMSs.[80] On the other hand, the MOF activation via solvent-assisted ligand exchange (SALE) was widely used as facial and efficient top-down method to expose the CUMSs.[72] The removal of coordinated solvent molecule (e.g., dimethylformamide) via solvent extraction will leave abundant CUMSs on the ultimate material.[40, 81] During the

extraction process, the rigidity of MOFs is able to prevent CUMSs from occluding.[82] Plasma engraving is another promising strategy for catalysts improvement (section 2.4.5). The previous work inspires the further fine control of CUMSs on the partially coordinated MOF candidates.

In the present study, Co-MOF-74 was selected as the starting material due to its intrinsic CUMSs and atomically dispersed metal centres.[40, 81a] In order to fine-tune its electro-catalytic activity toward OER, the microwave-induced plasma treatment was performed on Co-MOF-74 with designed treatment conditions (e.g., duration and power) and species (Figure 4-1). Even though plasma is a complex mixture (consisting of molecules, radicals, photons, etc.),[83] the most effective components of plasma in this research (the non-thermal plasma under low pressure gas) are possibly electrons and ions generated from the carrier gases. The high-density electrons bombardment can break the coordinate bonds between metal and organic ligands which may form engraved CUMSs.[84] At the same time, cations may determine the incorporation of defects (e.g., dangling ligand or ligand-vacancy defects on the surface),[85] depending on the carrier gas species. To optimise the active sites for catalysis, the defects in MOF are expected to be well controlled for exposing extra CUMSs while maintaining structural integrity. The relationship between their OER activities and CUMSs contents will be elucidated as well.

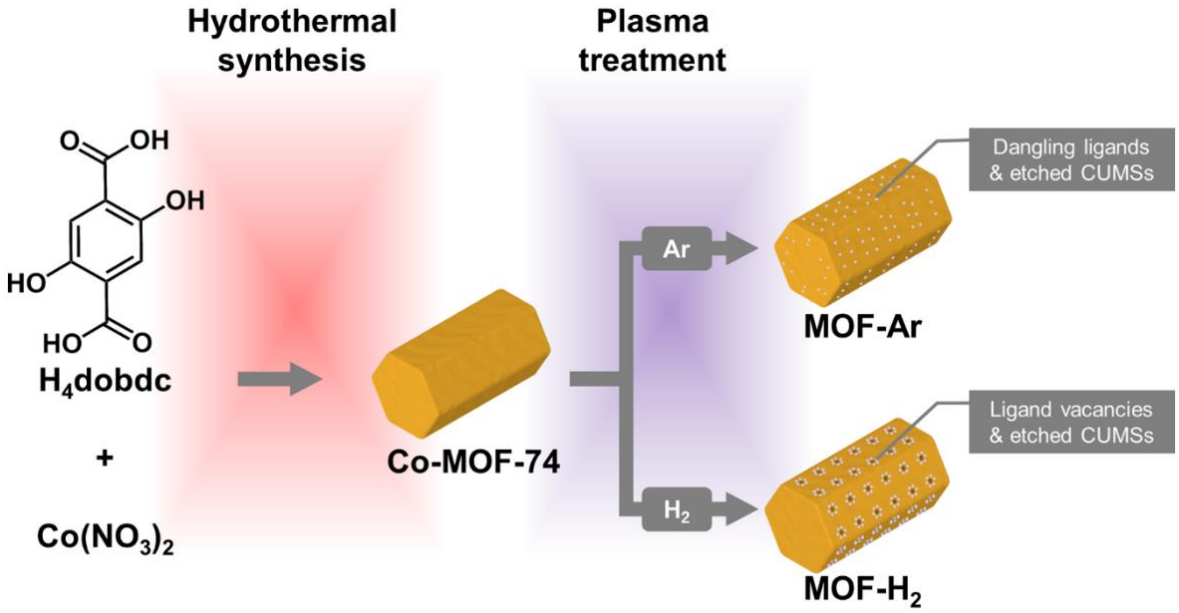


**Figure 4-1.** Scheme of preparation catalysts over argon and hydrogen plasma treatments.

### 4.2. Results and discussion

As described in section 3.1, the pristine **MOF** was synthesised in conformity to the previous studies,[40, 86] followed by plasma engraving. The MOFs engraved by argon and hydrogen plasma at an optimal treatment duration of 13 min and a power of 100 W are named as "**MOF-Ar**" and "**MOF-$H_2$**", respectively. The samples engraved with specific durations or power other than the optimal conditions have been added a suffix to show its conditions.

In order to investigate the effect of plasma treatment on the crystal structure of MOFs, X-ray diffraction (XRD) was conducted. The X-ray diffractograms (patterns) of simulated Co-MOF-74 and synthesised MOF are shown at the bottom of Figure 4-2a, while the two patterns at the top are the MOF-Ar and MOF-$H_2$ obtained by the plasma treatment. All of them present sharp peaks at 6.8° and 11.8° corresponding to the (110) and (300) planes in rhombohedral systems respectively.[86a] The high similarity of crystal structures is noticed between our synthesised MOF and simulated MOF, confirming the successful preparation of MOF. Meanwhile, no additional phase is observed after plasma treatments under the two carrier gases. However, MOF-$H_2$ displays lower peak intensities, which may indicate the decline of crystallinity, contraction of the unit cell or formation of defects through plasma treatments.[14, 87] In the meantime, different duration and power of argon and hydrogen plasma were applied on MOFs in order to investigate their effects on creating CUMSs. Although extra defects may be introduced with the increment of treatment duration or power, it is found that the unique MOF structure would collapse by excessive plasma treatment (Figure 4-3) after optimal duration (13 min) and power (100 W).[14] Since MOF is expected to maintain its porous structure, further investigation would be performed under the optimal conditions.

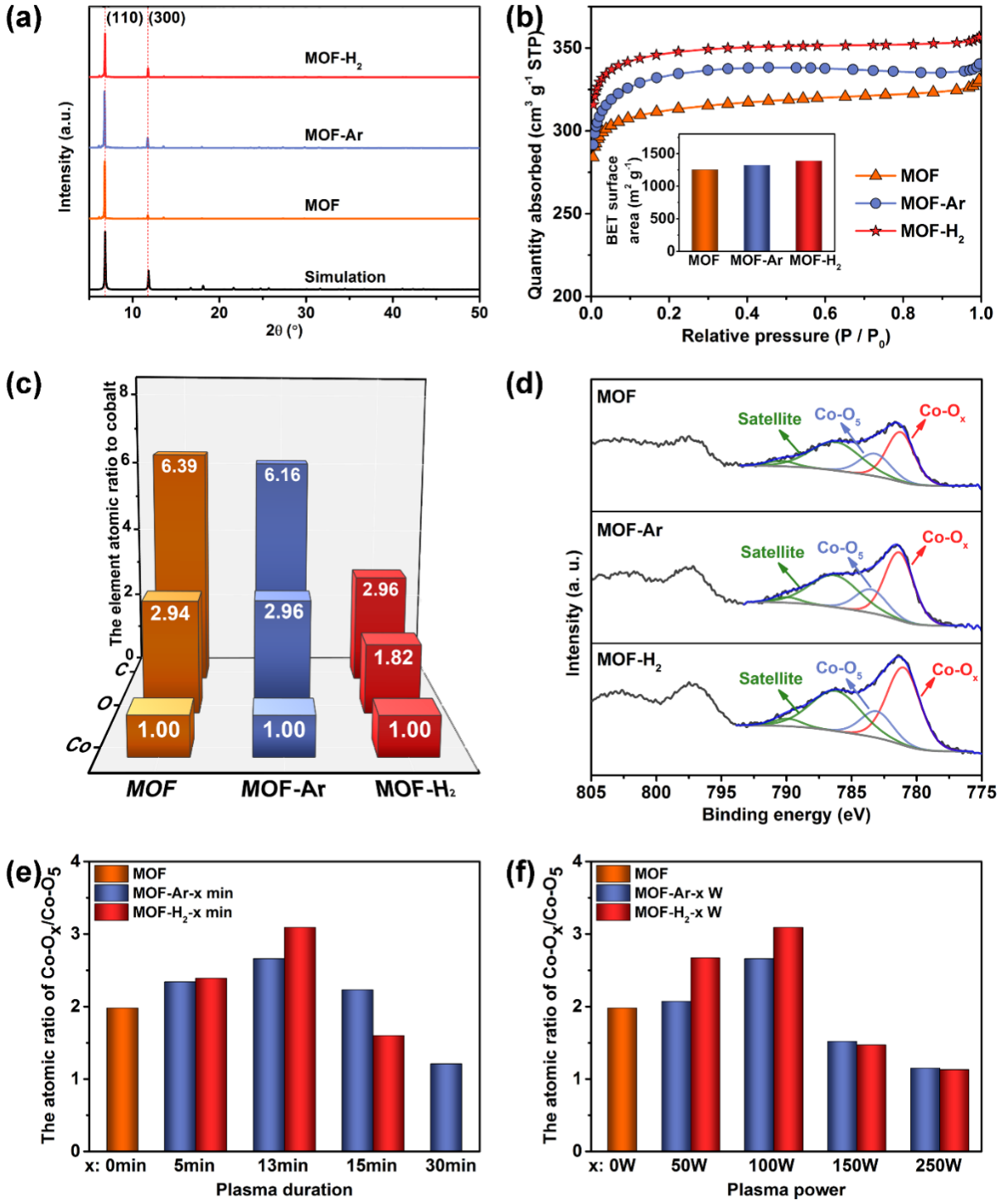


**Figure 4-2.** (a) X-ray diffraction (XRD) diffractograms (patterns) for simulated Co-MOF-74, MOF, MOF-Ar and MOF-$H_2$. MOF-Ar and MOF-$H_2$ were engraved at 100 W for 13 min under argon and hydrogen atmospheres separately. (b) Nitrogen sorption isotherms for MOF, MOF-Ar and MOF-$H_2$. Inset: surface areas estimated through Brunauer Emmett Teller (BET). (c) The surface elements atomic ratios to Co measured by X-ray photoelectron spectra (XPS). (d) Co 2p spectra. (e) The atomic ratio of Co-$O_x$/Co-$O_5$ for plasma engraved MOFs over different duration at 100 W and (f) plasma

engraved MOFs over different power at 13 min.

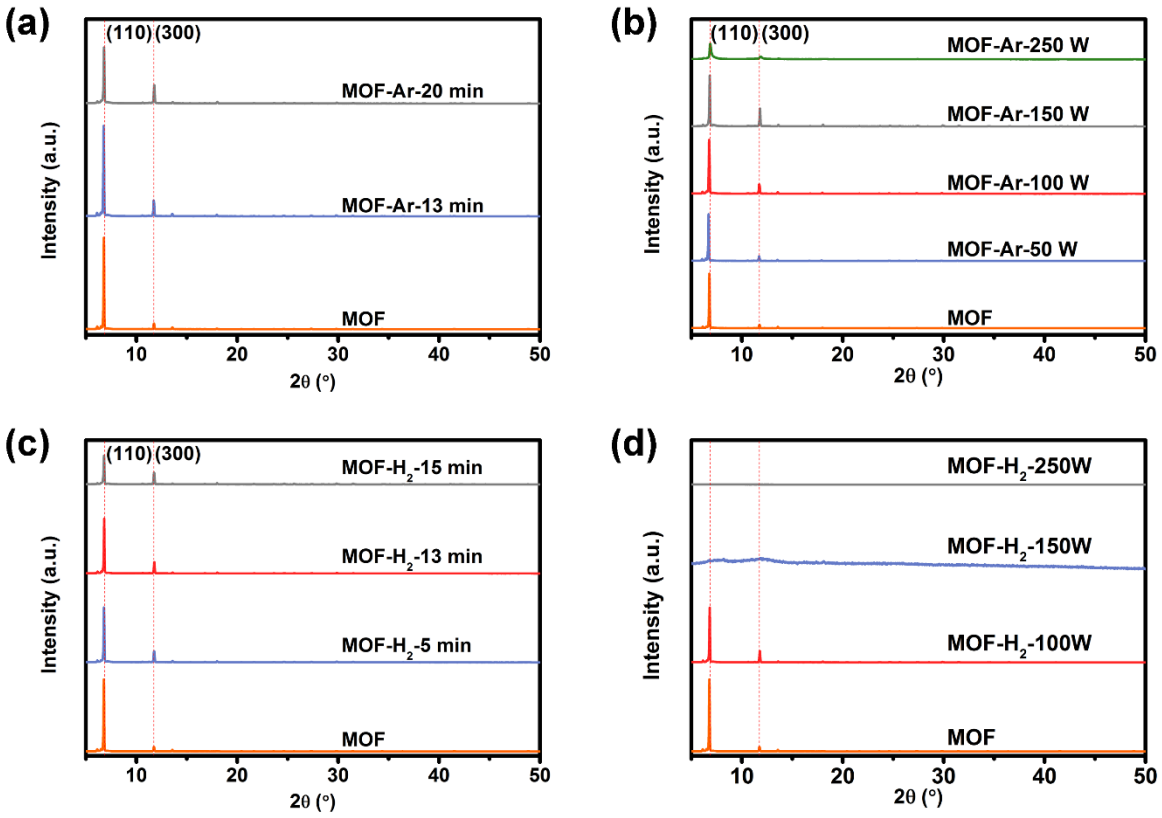


**Figure 4-3.** X-ray diffraction (XRD) patterns for (a) argon plasma engraved MOFs over different duration at 100 W, (b) argon plasma engraved MOFs over different power at 13 min, (c) hydrogen plasma engraved MOFs over different duration at 100 W and (d) hydrogen plasma engraved MOFs over different power at 13 min.

Fourier-transform infrared spectroscopy (FTIR) spectra are shown in Figure 4-4. For pristine MOF and plasma engraved MOFs, the feature at 1241 $cm^{-1}$ is related to the C-N, which may be ascribed to the solvent of DMF.[86b, 88] For the organic ligand of MOF, the features at 1542 $cm^{-1}$, 1195 $cm^{-1}$, and 1404 $cm^{-1}$ can be assigned to the vibration of C=O, C-O (carboxylic group), and C=C (aromatic hydrocarbons), respectively. The peaks at 883 and 812 $cm^{-1}$ are assigned to the C-H in benzene ring. The good matching of absorption peaks positions among the catalysts demonstrate the negligible change in the functional groups of MOFs after plasma treatments.

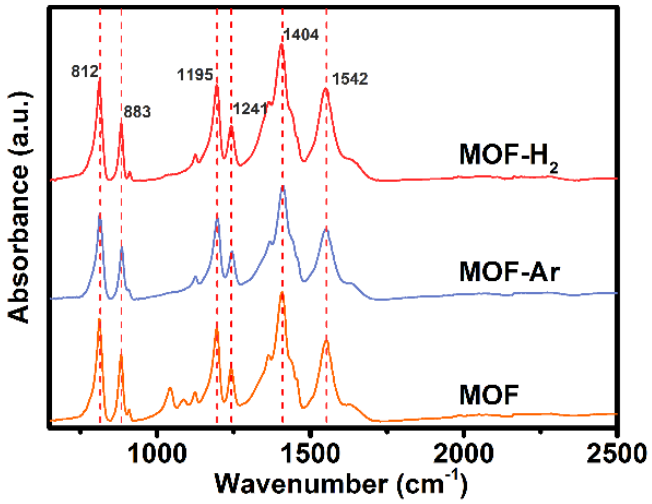


**Figure 4-4.** Fourier-transform infrared spectroscopy (FTIR) spectrums for MOF, MOF-Ar and MOF-$H_2$.

The surface morphologies of catalysts were studied by scanning electron microscope (SEM) images (Figure 4-5). Compared with MOF (Figure 4-5a), even though the surface of MOF-$H_2$ becomes rougher (Figure 4-5c), its hexagonal structure (Figure 4-5d) is well preserved under plasma engraving. A similar result is also noticed on MOF-Ar (Figure 4-5b).

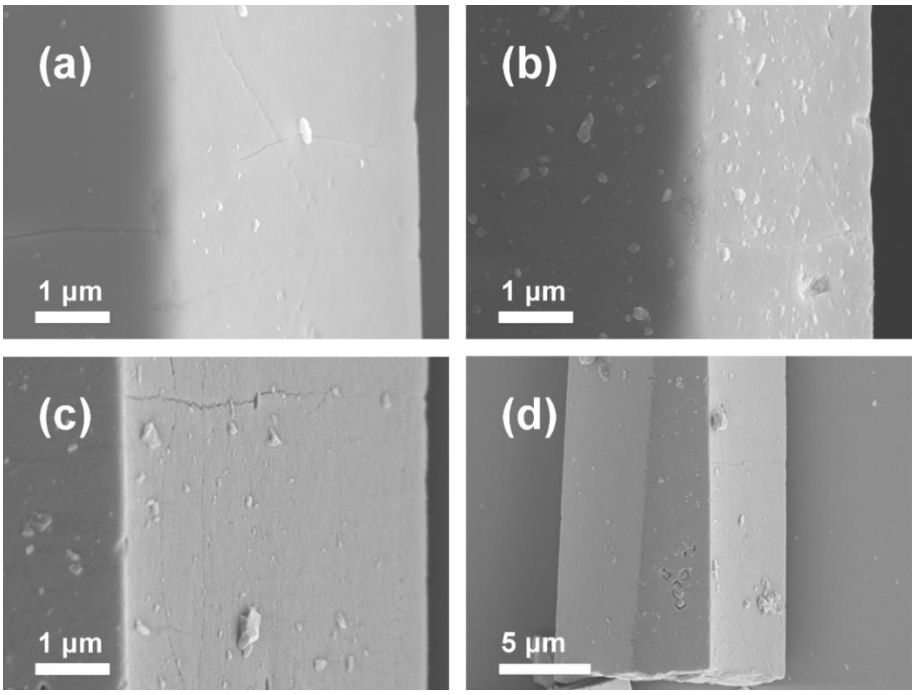


**Figure 4-5.** Scanning electron microscope (SEM) images for (a) MOF, (b) MOF-Ar and (c, d) MOF-$H_2$.

Due to possible crystal constriction, metal aggregation may occur and limit their performance. Thus, the transmission electron microscope (TEM) was applied to observe the interior metal dispersion of

the materials (Figure 4-6). Figure 4-6c shows the high resolution TEM image of MOF-$H_2$ indicating the absence of metal aggregation. Moreover, the energy dispersive X-ray (EDX) mapping confirms a good dispersion of C, O, and metal centres (Co) in the catalysts over plasma treatments. The maintained structures are consistent with the results of DBD plasma treated ZIF-67.[14] The results of XRD, FTIR, SEM, TEM and EDX mapping suggest that the bulk structure and composition of MOF are well reserved after short-term argon and hydrogen plasma treatments.

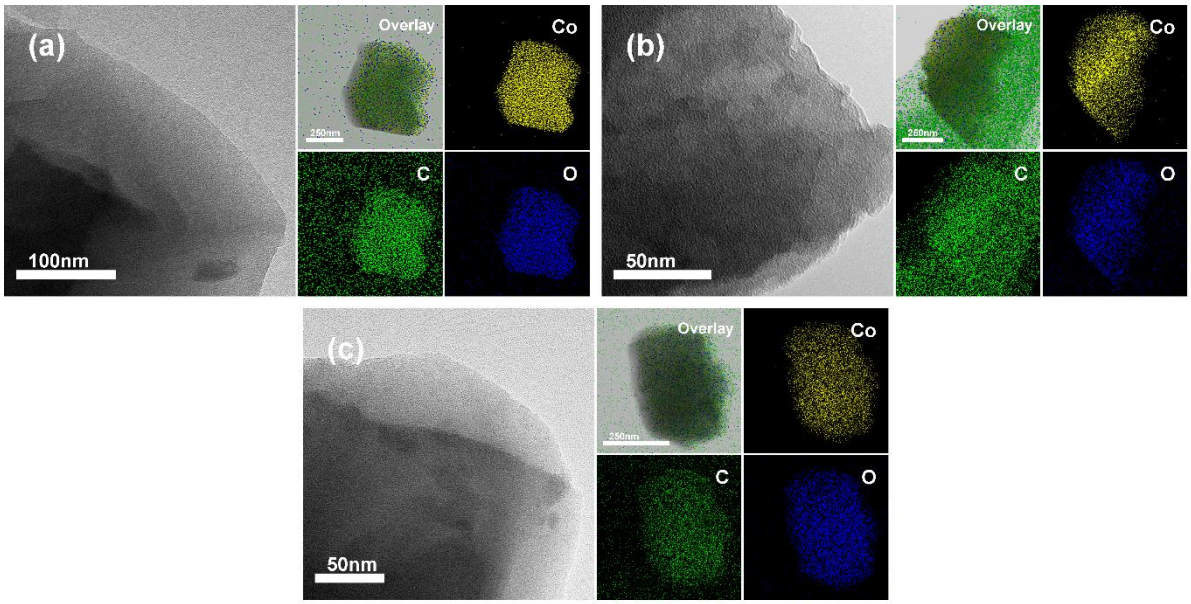


**Figure 4-6.** Transmission electron microscope (TEM) images and energy dispersive X-ray (EDX) mappings for (a) MOF, (b) MOF-Ar and (c) MOF-$H_2$.

Figure 4-2b shows the nitrogen sorption isotherms of the catalysts. the porous structures of MOFs can be maintained after plasma treatments, and their BET surface areas were even increased to different extents by argon and hydrogen plasma engraving (from pristine 1252 $m^2\ g^{-1}$ to 1323 $m^2\ g^{-1}$ and 1390 $m^2\ g^{-1}$, respectively). The increment of measured surface area after plasma treatment should be mainly due to the effective engraving and the formation of defects. Consequently, the existence of defects can facilitate the efficient removal of guest molecular and the improvement of pore accessibility, thereby enhancing their surface areas.

X-ray photoelectron spectra (XPS) were obtained to investigate the coordination geometry and elemental content of the catalyst surface. The proportion of elements (C, O, and Co) on the surface was measured by the general survey spectra of XPS (Figure 4-7). Because the Co metal atoms can hardly be removed by plasma treatment and its content can be seen as a constant value, the content

changes of C and O are studied with their atomic ratios to Co (Figure 4-2c). Compared with MOF, the C and O contents of MOF-Ar show no significant variation. Even though the MOF is engraved by argon plasma treatment, the terminated ligands probably dangle on the material's surface owing to the inertness of the noble gas atoms.[85a] In sharp contrast, the proportions of C and O on the surface of MOF-$H_2$ are decreased by about 38% and 54% respectively. This phenomenon explains its BET surface area improvement, namely, the active hydrogen ions ($H_3^+$) removed ligands and introduced defects on the surface.[89] The peaks assigned to C-O ($\approx$ 286.7 eV) are fitted in the C 1s spectra and their contents are shown as the atomic ratios to Co (Figure 4-8).[90] The decline of C-O peak after argon and hydrogen plasma engraving can be attributed to the damaged ligands. To investigate the coordination state of metal active centre, the peaks of Co-$O_x$ ($\approx$ 781.1 eV, $x < 5$), Co-$O_5$ ($\approx$ 783.3 eV) and two satellite peaks are fitted in the Co $2p_{3/2}$ spectra (Figure 4-2d).[14] The Co-$O_5$ peak is attributed to the cobalt atom coordinating with five oxygen atoms, which mainly exists in MOF after solvent extraction, and the Co-$O_x$ peak is attributed to the engraved unsaturated cobalt species. The existing Co-$O_x$ peak in MOF is probably caused by the unsaturated sites on the external surface or edges. Due to the facilitation of low coordinated cobalt (Co-$O_x$) toward OER, a large ratio of Co-$O_x$/Co-$O_5$ is highly demanded in the catalyst. The Co-$O_x$/Co-$O_5$ ratios of argon and hydrogen plasma engraved MOFs over different conditions are shown in Figure 4-2e and f. It is noteworthy that the ratio could reach up to 2.66 (MOF-Ar) and 3.09 (MOF-$H_2$) from 1.98 (MOF) by the plasma treatments over optimal power and duration. The volcano type curve suggests that the coordination geometry of metal centres can be controlled by plasma engraving. The existence of maximised CUMSs can be tailored when MOF phase integrity is maintained. By further extending treatment duration or increasing plasma power, the obvious reductions of the ratios demonstrate the partial or full structure collapse (Figure 4-3). With the reduced proportions of coordination ligand and the increased ratio of Co-$O_x$/Co-$O_5$, the induced structure defects and CUMSs by controllable plasma engraving are expected to further enhance OER activity.

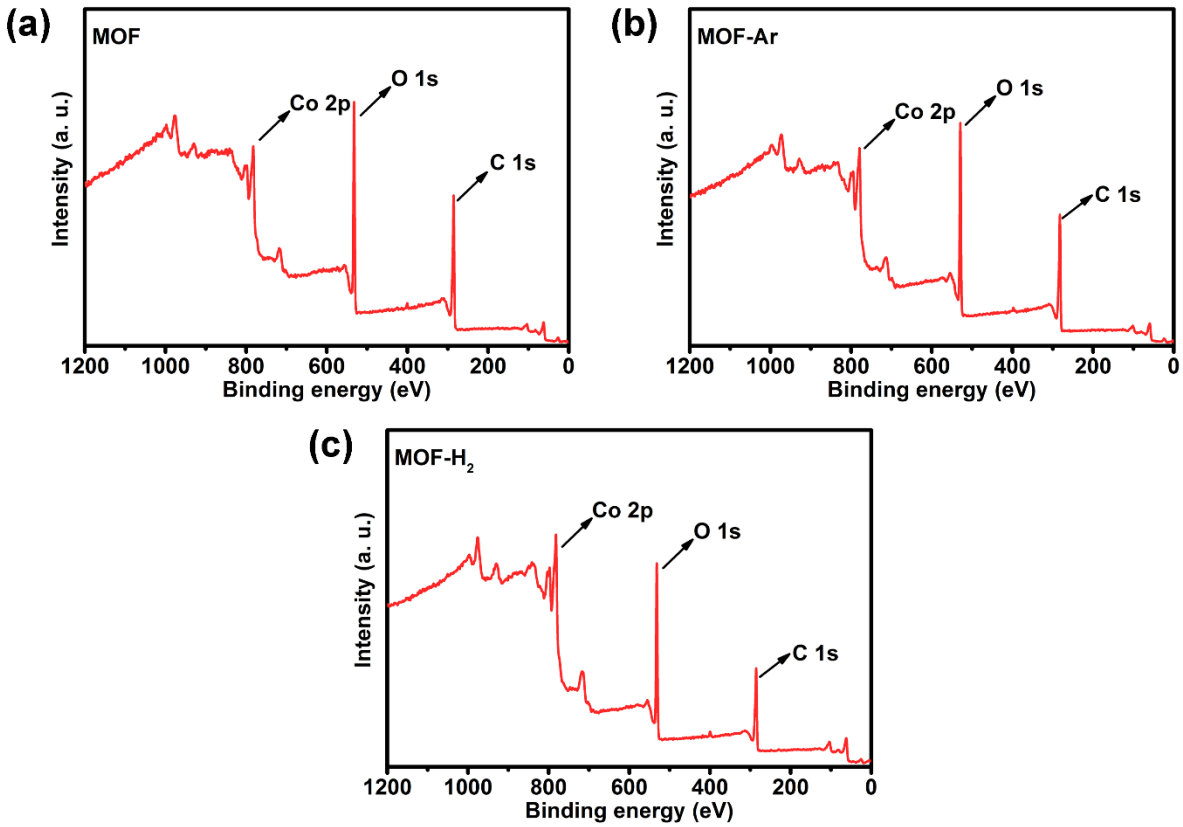


**Figure 4-7.** XPS survey spectra for (a) MOF, (b) MOF-Ar and (c) MOF-$H_2$.

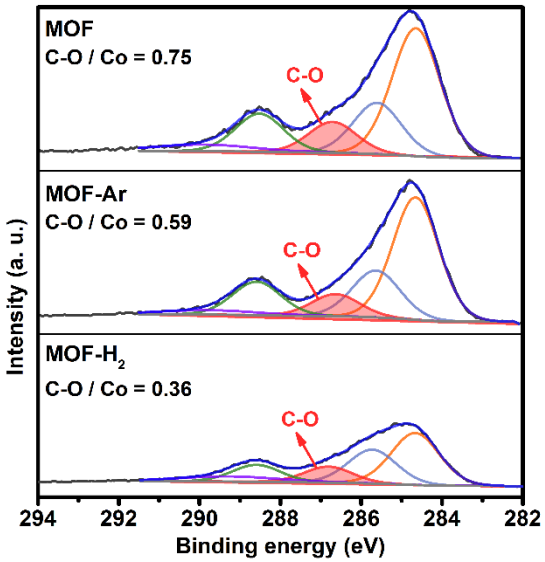


**Figure 4-8.** XPS C 1s spectra for MOF, MOF-Ar and MOF-$H_2$.

The coordination states of the catalysts were further demonstrated by X-ray absorption spectra (XAS) measurement. Due to the limited synchrotron beamtime, only pristine MOF and optimal MOF-$H_2$ were characterised and compared. The X-ray absorption near edge structure (XANES) spectra of Co

K-edge (Figure 4-9a) show that the rising edge of MOF-$H_2$ shifts to higher energy from MOF. This phenomenon exhibits the slight oxidation of MOF-$H_2$ since it exposed to the air with suspended bonds during sample collection after effective engraving.[14, 91] In order to reveal the variation of coordination environments, Fourier transforms of the $k^3$-weighted extended X-ray absorption fine structure (FT-EXAFS) oscillations in R-space (Figure 4-9b) were fitted (the fitting details are shown in Figure 4-9c, d and Table 4-1). The main peak at about 1.5 Å (all the distances in Figures and discussion are apparent distances without phase correction) is attributed to Co-O coordination, while the peak at 2.6 Å indicating Co-C or Co-Co coordination.[91] In consequence, the cobalt coordination number of MOF decreases from 4.5 to 4 after hydrogen plasma treatment (Figure 4-9e). This result crucially demonstrates the creation of defects and additional CUMSs by hydrogen plasma treatment as shown in the schematic diagram (Figure 4-10).

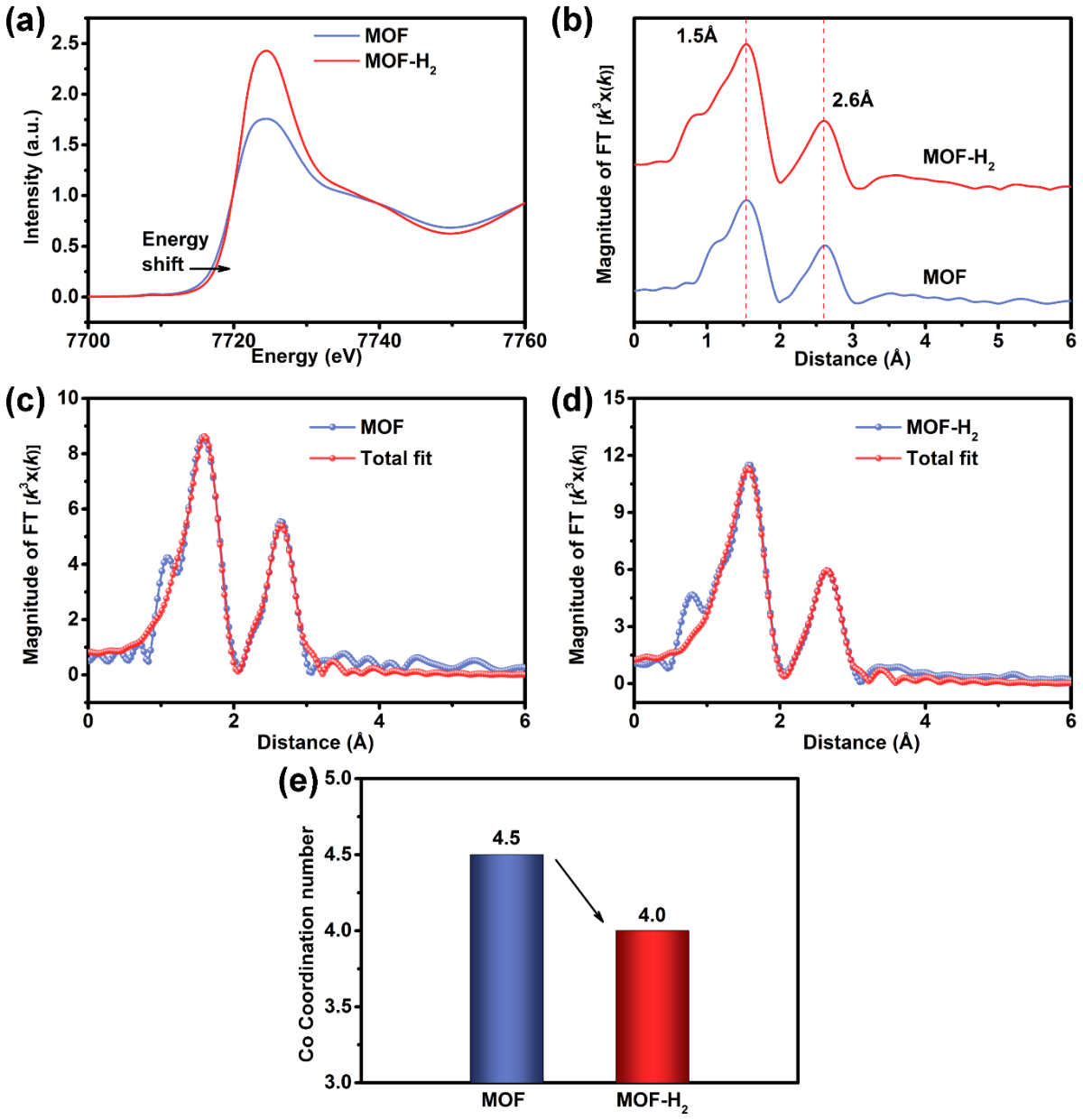


**Figure 4-9.** (a) Co K-edge X-ray absorption near edge structure (XANES) spectra for MOF and MOF-$H_2$. (b) The extended X-ray absorption fine structure (EXAFS) oscillations in Co R-space. The fitting of $k^3$-weighted Fourier transform EXAFS spectra of the Co K-edge for (c) MOF and (d) MOF-$H_2$. (e) Co coordination numbers.

**Table 4-1.** The EXAFS fitting parameters for MOF and MOF-$H_2$.

| Samples | Shell | C.N. | $\sigma^2(10^{-3}Å^2)$ | R(Å) |
|---|---|---|---|---|
| MOF | Co-O1[a)] | 4.5 | 7.4 | 2.052 |
| | Co-C1[a)] | 1.0 | 2.4 | 2.887 |
| | Co-Co1[a)] | 2.0 | 6.3 | 3.028 |
| MOF-$H_2$ | Co-O1[a)] | 4.0 | 3.4 | 2.052 |
| | Co-C1[a)] | 1.0 | 2.4 | 2.877 |
| | Co-Co1[a)] | 2.0 | 7.7 | 3.033 |
| | Co-Co2[b)] | 2.0 | 3.1 | 3.388 |

[a)] refers to cobalt MOF; [b)] refers to cobalt oxide.

The above results and analysis give solid evidence of our assumption about the effect of plasma engraving on MOFs' structure. Plasma treatment can effectively engrave materials as reported previously.[73, 92] As shown in the results of XPS and EXAFS, the Co-O bonds between metal centres and organic ligands are partially broken to expose extra CUMSs with the decrement of coordination number. The coordinated organic ligands are also damaged by plasma engraving to form complex defects that depend on the atmosphere. The argon plasma engraving is considered as the impact of electrons and argon ions.[84] Due to the relatively large size and inertness of argon atoms, the cations probably combine with existing electrons and recover to noble gas immediately after discharging and then leave the energetic field.[84a] Thus, most of the terminated organic ligands would still dangle on MOF surface and only partial active sites would be exposed to absorb reactants. As a result, MOF-Ar is expected to see a slight improvement in its electro-catalytic activity. With respect to hydrogen plasma engraving, the major cation of $H_3^+$ has a relatively small size and mass, which would be endowed with high kinetics and collisional energy by microwave.[89] The cations would destruct through protons transfer,[93] and thereafter, the terminated ligands might be extracted to form hydrocarbons and flow out via vacuum pumping (Figure 4-10). Thus, MOF-$H_2$ should expose more CUMSs around ligand vacancies and present higher activity than the former.

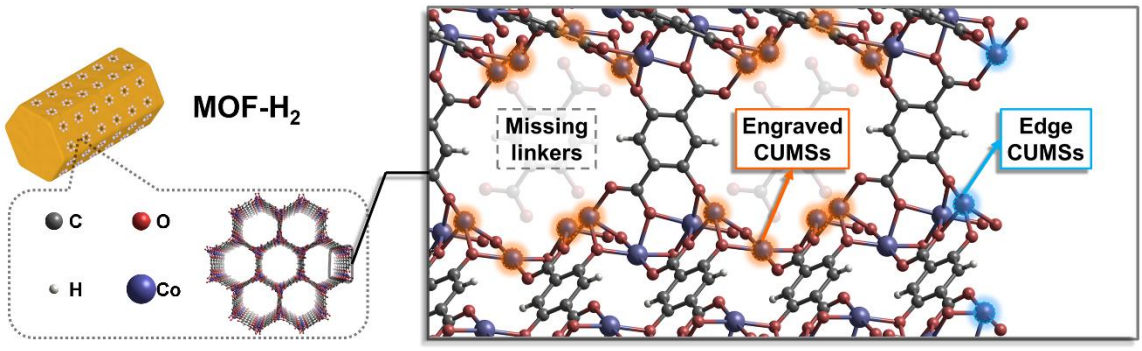


**Figure 4-10.** The schematic diagram of hydrogen plasma engraved MOF.

According to Figure 4-11a, the OER activities of MOF, MOF-Ar, MOF-$H_2$ and commercial $RuO_2$ were shown by linear sweep voltammetry (LSV) with the scan rate of 10 mV $s^{-1}$ in 0.1 $_M$ KOH, and all the three catalysts obviously outperform $RuO_2$. In addition, the redox peaks of their LSV curves clearly demonstrate the accessibilities of cobalt atoms. Compared with MOF, the stronger $Co^{2+}/Co^{3+}$ peaks of MOF-Ar and MOF-$H_2$ are obvious between 1.2 V to 1.3 V vs. RHE.[14, 94] This phenomenon demonstrates the increased proportions of accessible $Co^{2+}$ in the argon and hydrogen plasma engraved MOFs, which could be oxidised into $Co^{3+}$ and further transferred to $Co^{4+}$ during the OER process.[87a]

The effects of plasma treatment duration and power are further confirmed by OER performances through LSV curves (Figure 4-12). The overpotential at the current density of 15 mA $cm^{-2}$ can be used to express the electro-catalytic performance of OER catalyst, and a lower overpotential indicates its higher OER activity. The trends of OER activities with different plasma engraving conditions are easily observed in the overpotential, similarly in the TOF and mass activities at $\eta = 350$ mV. As shown in Figure 4-13a, b and c, most of plasma engraved MOFs have higher electro-catalytic activities than commercial $RuO_2$. The OER activities of catalysts are gradually improving with the increasing duration of argon and hydrogen plasma treatment. Nevertheless, the performances markedly decline after the optimal MOF-Ar-13 min and MOF-$H_2$-13 min. It is possibly due to the structural collapse and aggregated metal centres from excessive plasma treatment which are concluded through the XRD results (Figure 4-3). Similarly, the trend is observed through the catalysts over different power (Figure 4-13d, e and f). The 100 watts, which leads to the highest activity among argon and hydrogen plasma treated MOFs of various powers, is demonstrated as optimal intensity. More important, Figure 4-11d clearly exhibits the correlation between overpotential and the atomic ratio of Co-$O_x$/Co-$O_5$. This

quantitative correlation indicates the contribution of fine-tuned CUMSs to electro-catalytic activity as the active centres, which is confirmed by the trend of TOF (Figure 4-11e). As a result, the tuneable plasma engraving could effectively engrave CUMSs to target MOF by controllably introducing framework structure defects.

Among the studied samples in this part, MOF-$H_2$ shows the lowest overpotential (337 mV at 15 mA $cm^{-2}$), highest TOF (0.0219 $s^{-1}$) and largest mass activity (54.3 A $g^{-1}$). It means the hydrogen plasma engraving can successfully incorporate abundant defects of ligand vacancies into MOF and fine-tune CUMSs. MOF-Ar presents a moderate improvement of OER activity (overpotential of 354 mV at 15 mA $cm^{-2}$) from MOF, indicating that the dangling ligands of MOF-Ar still block the metal active centres from fully interacting with the electrolytes. Nevertheless, the activities of MOF-Ar and MOF-$H_2$ are promising even compared with other catalysts for OER (Table 4-2). Subsequently, their stabilities were tested at a current density of 10 mA $cm^{-2}$ for about 2.7 hours (Figure 4-11b), and all the catalysts show promising OER performance in 0.1 $_M$ KOH. In contrast, the remaining ligands over argon plasma treatment are able to prevent MOF-Ar from occluding CUMSs. The electrochemical impedance spectroscopy (EIS) of samples are recorded at a constant potential of 1.53 V vs RHE under OER conditions. According to the Nyquist plots (Figure 4-11c) of EIS, both of MOF-Ar and MOF-$H_2$ have almost the same charge transfer resistances and show improved conductivities compared with MOF. As their OER performances are obviously different, it is the fine-tuned CUMSs, instead of the charge transferability, that makes the major contribution to OER activity improvement.

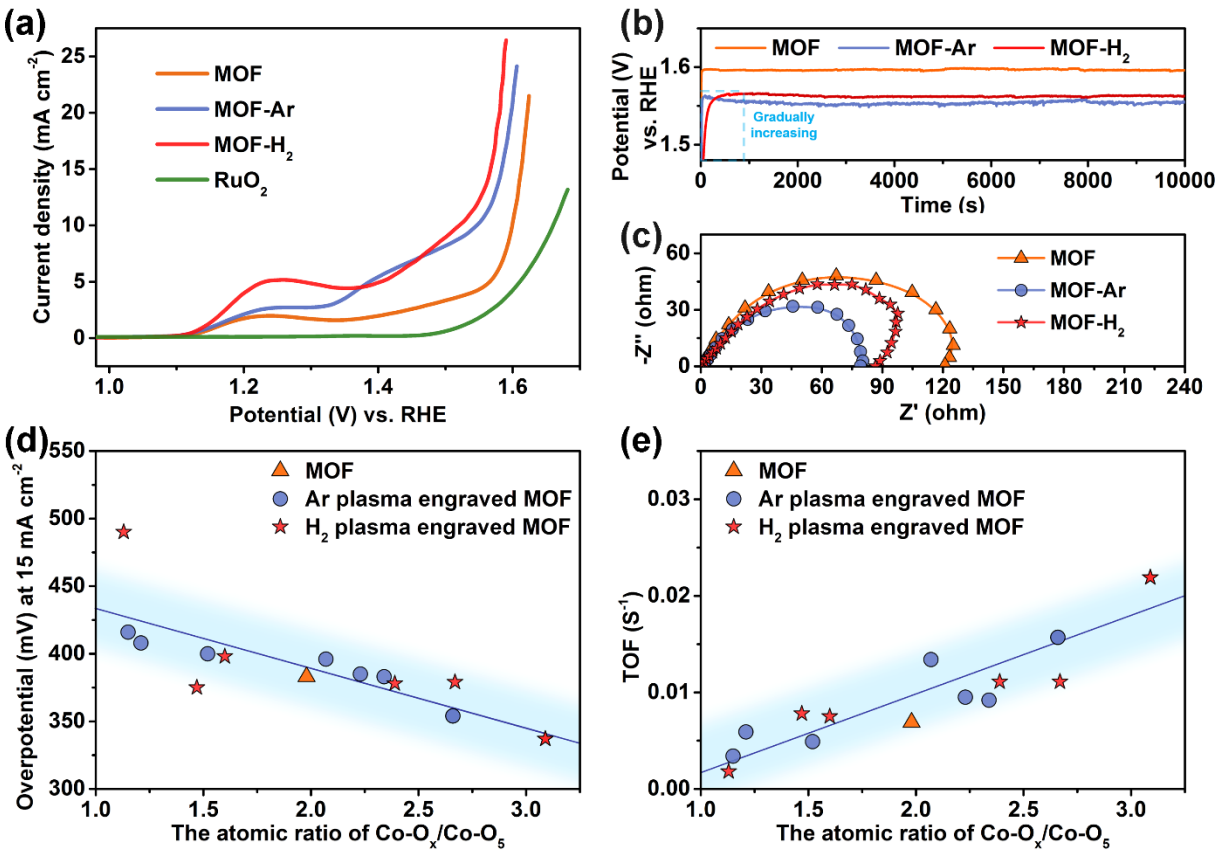


**Figure 4-11.** (a) Linear sweep voltammetry (LSV) curves for MOF, MOF-Ar, MOF-$H_2$ and commercial $RuO_2$ in 0.1 M KOH. MOF-Ar and MOF-$H_2$ were engraved at 100 W for 13 min under argon and hydrogen atmospheres separately. (b) Chronopotentiometry curves for MOF, MOF-Ar and MOF-$H_2$ at current density of 10 mA $cm^{-2}$. (c) Electrochemical impedance spectroscopy (EIS) analysis of catalysts at a constant potential of 1.53 V vs RHE. (d) The correlation between the overpotential at current density of 15 mA $cm^{-2}$ and $CoO_x/CoO_5$ atomic ratio of pristine and plasma engraved MOFs. (e) The correlation between the Turnover frequency (TOF) at $\eta$ = 350 mV vs RHE and $CoO_x/CoO_5$ atomic ratio.

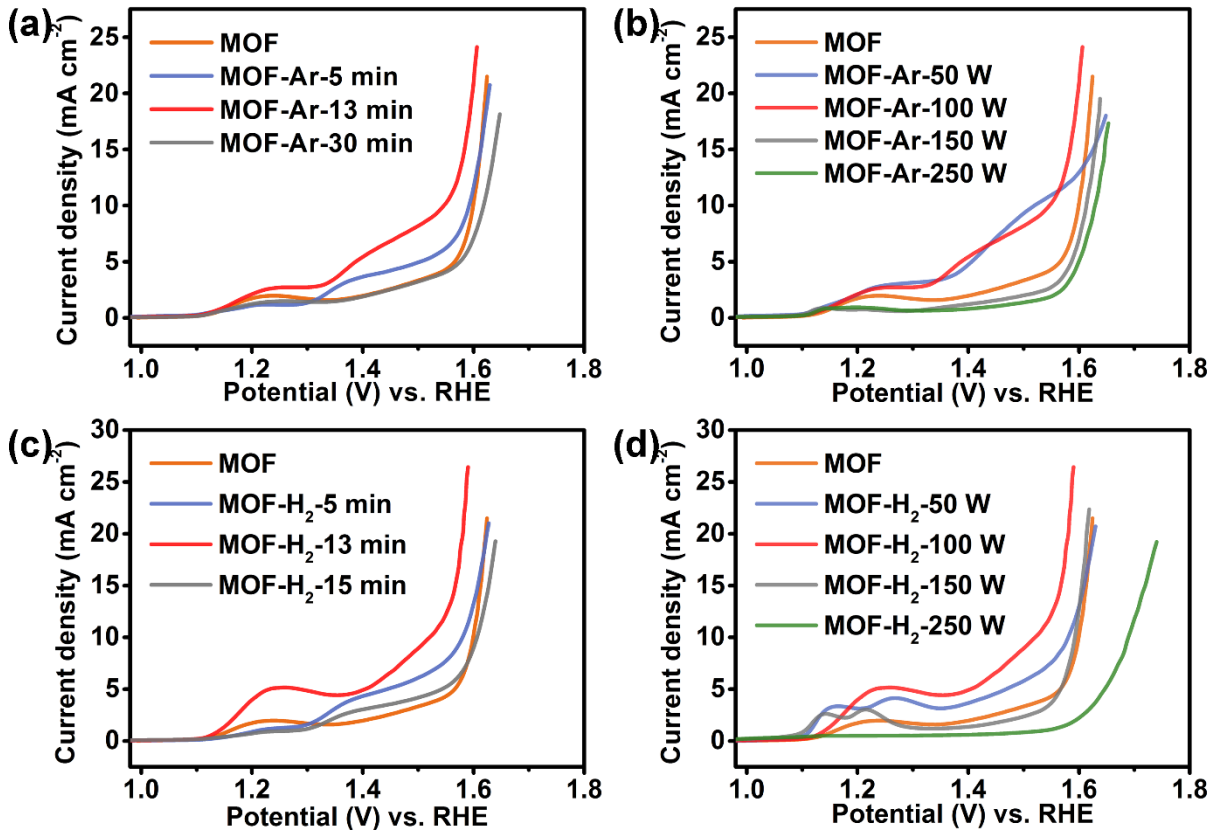


**Figure 4-12.** (a) Linear sweep voltammetry (LSV) curves in 0.1 $_{M}$ KOH for (a) argon plasma engraved MOFs over different duration at 100 W. (b) argon plasma engraved MOFs over different power at 13 min. (c) hydrogen plasma engraved MOFs over different duration at 100 W and (d) hydrogen plasma engraved MOFs over different power at 13 min.

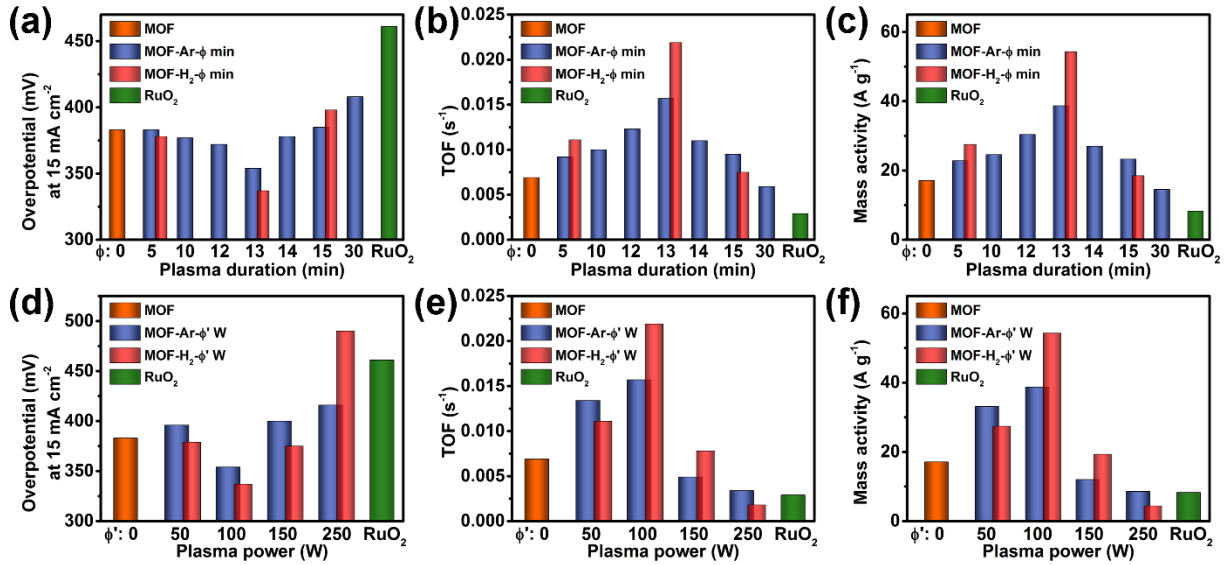


**Figure 4-13.** (a) Overpotential at current density of 15 mA cm$^{-2}$ for argon and hydrogen plasma engraved MOFs over different duration at 100 W and commercial $RuO_2$. (b, c) Turnover frequency (TOF) and mass activity at $\eta$ = 350 mV vs

RHE. (d, e, f) Overpotential, TOF and Mass activity for plasma engraved MOFs over different power at 13 min and commercial $RuO_2$.

**Table 4-2.** The list of overpotential for MOF-based catalysts tested in OER catalysis.

| Material | Overpotential (mV) | Measured Current Density (mA $cm^{-2}$) | OER Electrolyte (KOH) | Reference |
|---|---|---|---|---|
| Co-MOF-74 | 383 | 15 | 0.1 M | This thesis |
| MOF-Ar | 354 | 15 | 0.1 M | This thesis |
| MOF-$H_2$ | 337 | 15 | 0.1 M | This thesis |
| Co-ZIF-67 | 400 | 10 | 1 M | [14] |
| DBD Plasma treated ZIF-67 | 320 | 10 | 1 M | [14] |
| NiCo-BDC | 317 | 10 | 1 M | [11b] |
| $Fe_3$-$Co_2$-MOF | 283 | 10 | 0.1 M | [95] |
| NiFe-NDC | 318 | 10 | 0.1 M | [54] |

In addition, methane plasma treatment has also been carried out and named as "MOF-$CH_4$". MOF-$CH_4$ shows the decline of crystallinity that may be due to the formation of amorphous species (Figure 4-14a). MOF-$CH_4$ has a relatively high ratio of Co-$O_x$/Co-$O_5$ that achieves to 3.83 from the 1.98 of MOF (Figure 4-14Left). However, the carbon proportion (Figure 4-14Right) of MOF-$CH_4$ reaches two times higher than MOF (C/Co ratio from 6.39 to 14.35). Therefore, even though MOF-$CH_4$ was engraved with extra CUMSs, the $CH_4$ might decompose on metal sites during $CH_4$ treatment, and thus the potential carbon deposition would partially block metal sites from contacting with reactant. The blockage of pore accessibility is also verified by BET result as its surface area dramatically reduces to 726 $m^2$ $g^{-1}$ (Figure 4-14c). As a result, MOF-$CH_4$ shows a poor electro-catalytic activity with overpotential of 400 mV at 15 mA $cm^{-2}$ that is seriously limited by carbon deposition Figure 4-14d). Consequently, the $CH_4$ plasma treatment would restrict the OER activity of MOF via carbon deposition, instead of fine-tuning its CUMSs content to boost the activity.

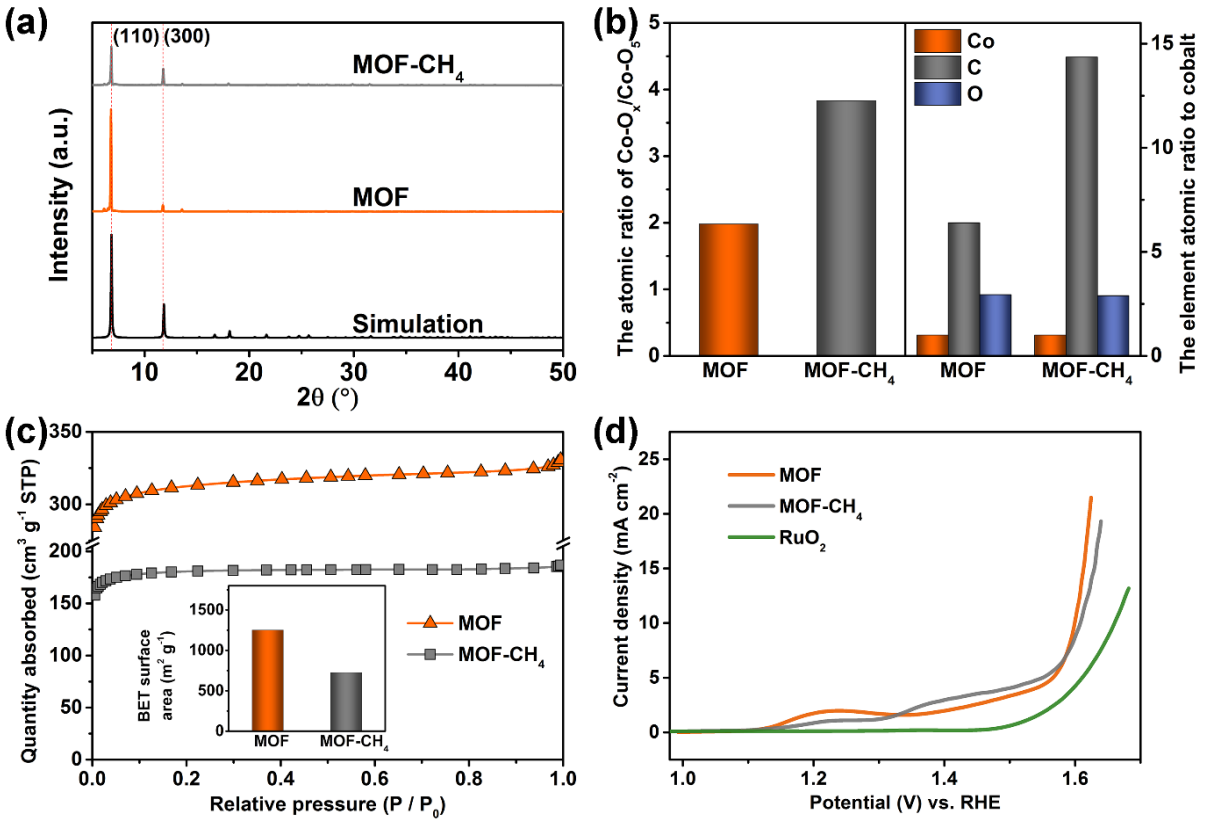


**Figure 4-14.** (a) XRD patterns for simulated Co-MOF-74, MOF and MOF-$CH_4$. MOF-$CH_4$ was engraved at 100 W for 13 min under methane atmosphere. (b) The atomic ratio of Co-$O_x$/Co-$O_5$ (Left) and the surface elements atomic ratios to Co (Right) for MOF and MOF-$CH_4$ measured by XPS. (c) Nitrogen sorption isotherms. Inset: surface areas estimated through BET. (d) LSV curves for MOF, MOF-$CH_4$ and commercial $RuO_2$ in 0.1 $_M$ KOH.

### 4.3. Conclusion

In this study, a controllable strategy has been successfully established to introduce defects and extra CUMSs on Co-MOF-74. As expected, the microwave-induced plasma treatment presents an obvious engraving effect on the target MOF, whose structure and electrochemical properties can be controlled by the carrier gas, power and duration of plasma treatment. An insufficient plasma engraving will lead to negligible improvement, but however, an excessive plasma treatment with either over-long duration or over-high power is supposed to collapse the porous structure and reduce the electro-catalytic activities of MOFs. With the optimised conditions, the MOFs engraved with argon and hydrogen plasma show improved OER activities than MOF, which are attributed to the fine-tuning of CUMSs. MOF-$H_2$ with abundant defects and CUMSs achieves the lowest overpotential of 337 mV at 15 mA $cm^{-2}$ among all the samples in this study. On the other hand, MOF-Ar exhibits a moderate promotion of OER activity (overpotential of 354 mV at 15 mA $cm^{-2}$) and retain the stability from MOF.

In consequence, the plasma engraving offers a promising route to further enhance electro-catalytic activity on bulk MOFs by introducing defects and fine-tuning active metal centres. The revealed quantitative correlations of CUMSs enrichment and electro-catalytic activity will inspire the development of relevant materials for other applications such as adsorption, sensors, and a variety of catalytic reactions.

# Chapter 5. Enhancing Electro-catalytic Activity of Cobalt-based MOF Electrocatalysts with Graphene Oxide Intercalation

## 5.1. Introduction

Section 2.4.3 describes a promising route for improving electro-catalysts via material hybridisation. MOFs show the potential to be considered as the precursor, owing to their stable fabrication result and atomically dispersed metal centres. Petit et al. proved the successful synthesis of composite between Cu-BTC and graphene-based components, which exhibited the enhanced porosity from parent materials.[96] Travlou et al. further evidenced the morphology of composites that MOF components were embedded between exfoliated graphite-oxide layers under relatively high loading proportion of graphene-based phase.[5a]

In this study, graphene oxide (GO) was intercalated in Co-MOF-74 to form composites with the hierarchical structure. Firstly, the hydrophilic GO was uniformly dispersed in the ethanol-DMF mixed solvent, followed by the dissolving of needed $Co(NO_3)_2 \cdot 6H_2O$. Metal cations were hypothesised to contact well with the opened epoxide ring of GO through the formation of complexes so that organic ligands could be coordinated on the substrate. The MOF could be distracted by parallel GO layers during its self-assembly, and thus the fabricated composites presented hierarchical hexagonal morphology. Meanwhile, the porosity of MOF could be retained and even improved at a low loading proportion without inducing phase transformation or separation. Consequently, the sample with the optimal loading proportion of GO (MOF-20) exhibits the highest performance among all the catalysts in this study. It only needs the overpotential of 413 mV to achieve the current density of 15 mA $cm^{-2}$ in 0.1 $_M$ KOH. The mass activity reaches up to 75.3 A $g^{-1}$ at $\eta$ = 450 mV, which is 3.5 times higher than pristine MOF. This study provides a practical route to further tune the microstructure of bulk MOFs, which can promote their utilisation performances as super-capacitor, fuel cell electrode and electrocatalysts for other reactions.

## 5.2. Results and discussion

In this study, **MOF** was synthesised in conformity to section 3.1. GO was dispersed in the solution during the synthesis of MOF to fabricate MOF/GO composites. The samples intercalated with GO are named as "**MOF-X**", where "X" indicates the specific weight percent of GO participating in the synthesis.

Figure 5-1a shows the X-ray diffraction (XRD) patterns of GO, MOF and MOF/GO composites with different loading proportions. GO is an amorphous material; therefore no peaks can be observed in its XRD pattern. By contrast, all the MOF composites exhibit sharp peaks at 6.8° and 11.8° (Card Number: 00-063-1147), which indicates that the crystal structure of MOF can be retained after GO intercalation. However, their peaks intensities decrease continuously with the increasing loading proportions of GO, which may be attributed to the successful intercalation of amorphous GO or the contraction of unit cell.

The Fourier-transform infrared spectroscopy (FTIR) spectra of samples are shown in Figure 5-1b. The broad band around 2000-3500 $cm^{-1}$ for GO is attributed to C-OH group,[5a, 63] while the feature at 1573 $cm^{-1}$ may be ascribed to the stretching vibration of C=O bonds in carbonyl and carboxylic groups and that at 1209 $cm^{-1}$ can be related to epoxy or peroxide groups. For MOF and MOF/GO composites, the broad band near 3338 $cm^{-1}$ indicates the absorbed water or methanol on the sample surface.[86b, 88] Meanwhile, the feature at 1241 $cm^{-1}$ is related to the C-N, which may be ascribed to the solvent of DMF. For the organic ligand of MOF, the features at 1542 $cm^{-1}$, 1195 $cm^{-1}$, and 1404 $cm^{-1}$ can be assigned to the vibration of C=O, C-O (carboxylic group) and C=C (aromatic hydrocarbons), respectively. The peaks at 883 and 812 $cm^{-1}$ are assigned to the C-H in benzene ring. The high similarity of these features indicates the retained MOF structure in different composites. The absorbance of spectrum increases with the growth of loading proportion, which indicates the successful intercalation of GO.

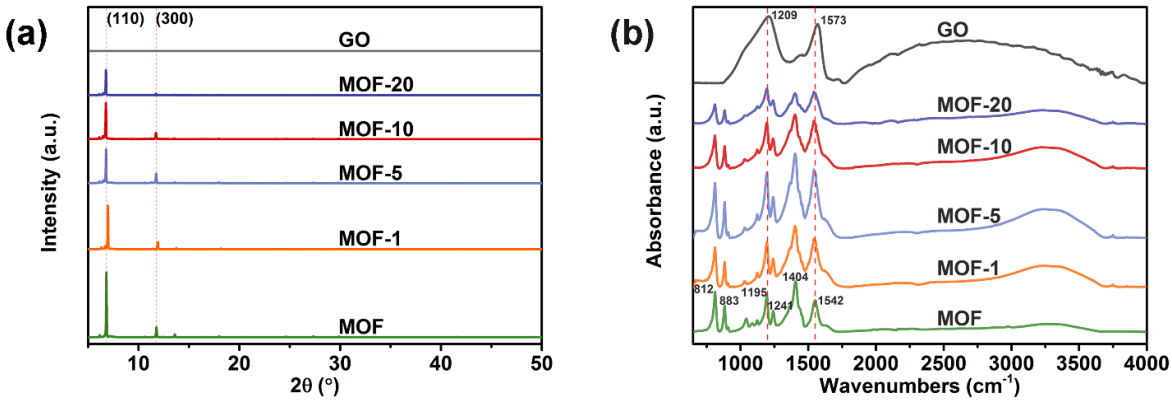


**Figure 5-1.** (a) X-ray diffraction (XRD) patterns for graphene oxide (GO), Co-MOF-74 and MOF/GO composites with different loading proportions. (b) Fourier-transform infrared spectroscopy (FTIR) spectra.

Raman spectroscopy was conducted under room temperature to investigate the vibrational modes of GO, MOF and MOF/GO composites. As shown in Figure 5-2, the feature of MOF and composites at 567 $cm^{-1}$ corresponds to the Co-O stretching modes, while the feature at 820 $cm^{-1}$ is assigned to C-H in the benzene ring. Besides, the C=O stretching is represented by the feature at 1275 $cm^{-1}$, and the O-C-O symmetric stretching of carboxylate group is displayed as the feature at 1502 $cm^{-1}$. The features of GO are not observed in the spectra of composites, owing to its relatively low proportion and embedded position. The good matching between MOF and composites demonstrates this practicable route for synthesis MOF with intercalated GO layers.

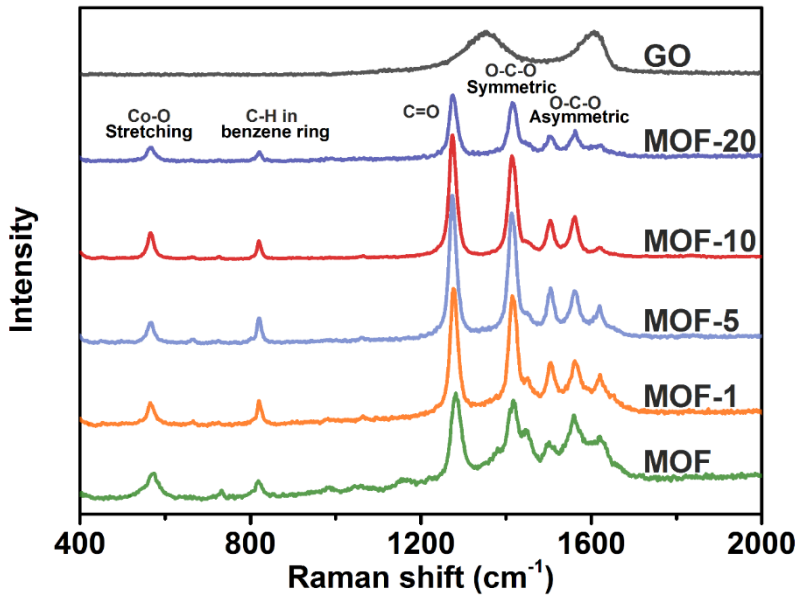


**Figure 5-2.** Raman spectra of GO, MOF and composites with different loading proportions at room temperature.

The morphology details of samples were investigated through scanning electron microscope (SEM) and their images are shown in Figure 5-3. The obvious hexagonal structure of MOF demonstrates the successful synthesis of Co-MOF-74.[7a, 40, 75, 86b] As seen from Figure 5-3b, MOF-1 retained the morphology of MOF with the similar particle size owing to the relatively low loading proportion of GO. The parallel interlayers verify the hierarchical intercalant between MOF layers. Moreover, additional structural defects are introduced with the increasing of GO loading, proven by the decrement of peaks intensities in XRD results (Figure 5-1a). The material extended from black interlayers appears as the laminar GO in Figure 5-3f. Accordingly, the hierarchical morphology of the composites should stem from the distraction of MOF during the fabrication process. The GO layers could act as conductive channels through MOF crystal, which might improve the exposal of active metal centres inside bulk MOF and also benefits to the electro-catalytic activity.

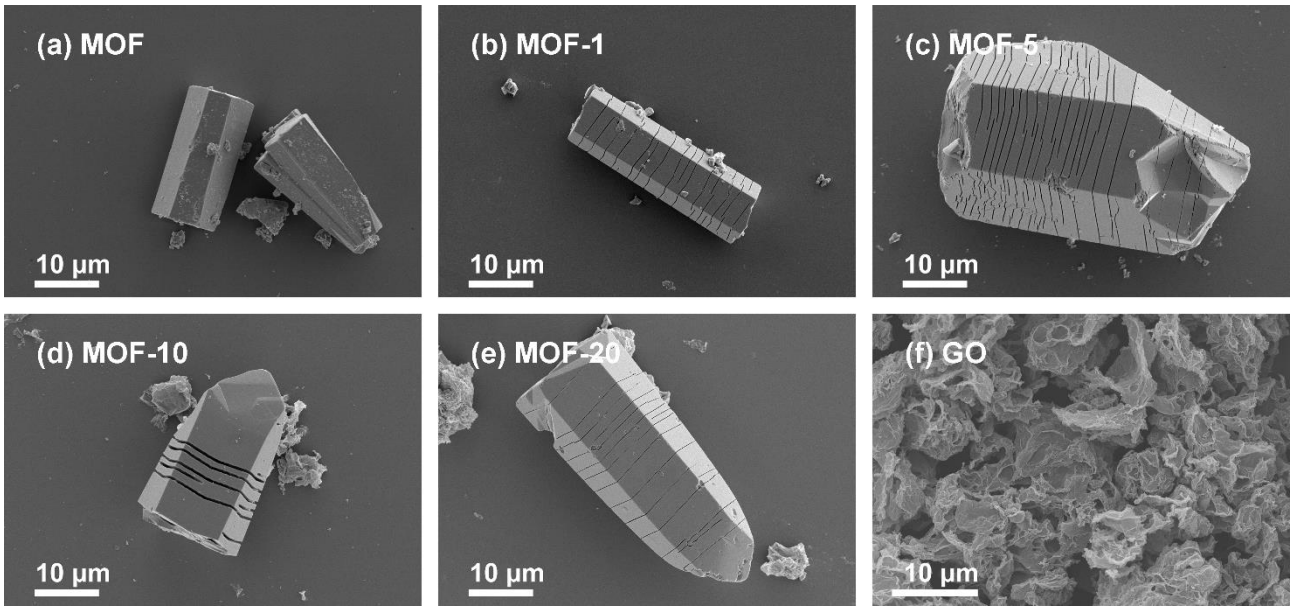


**Figure 5-3.** Scanning electron microscope (SEM) images for (a) MOF, (b) MOF-1, (c) MOF-5, (d) MOF-10, (e) MOF-20 and (f) GO.

X-ray photoelectron spectra (XPS) analysis was performed to collect the information of functional groups and elemental content present on samples' surface. The differences of functional groups are evidenced through the peak fitting of fine-scanned C 1s spectra for MOF/GO composites (Figure 5-4). According to Table 5-1, the percentage of aromatic C-C increases while the relative proportions of other groups decrease. This trend is likely contributed by the increased amount of intercalated GO. The proportions of elements on the surface of MOF-1 and MOF-20 were obtained by general survey

spectra of XPS (Figure 5-5a, b). The content of C and O are estimated by their atomic ratio to the content of Co (as shown in Figure 5-5c). Therefore, the successful intercalation of GO is proved by the large increment of C and the negligible change of O content on MOF-20.

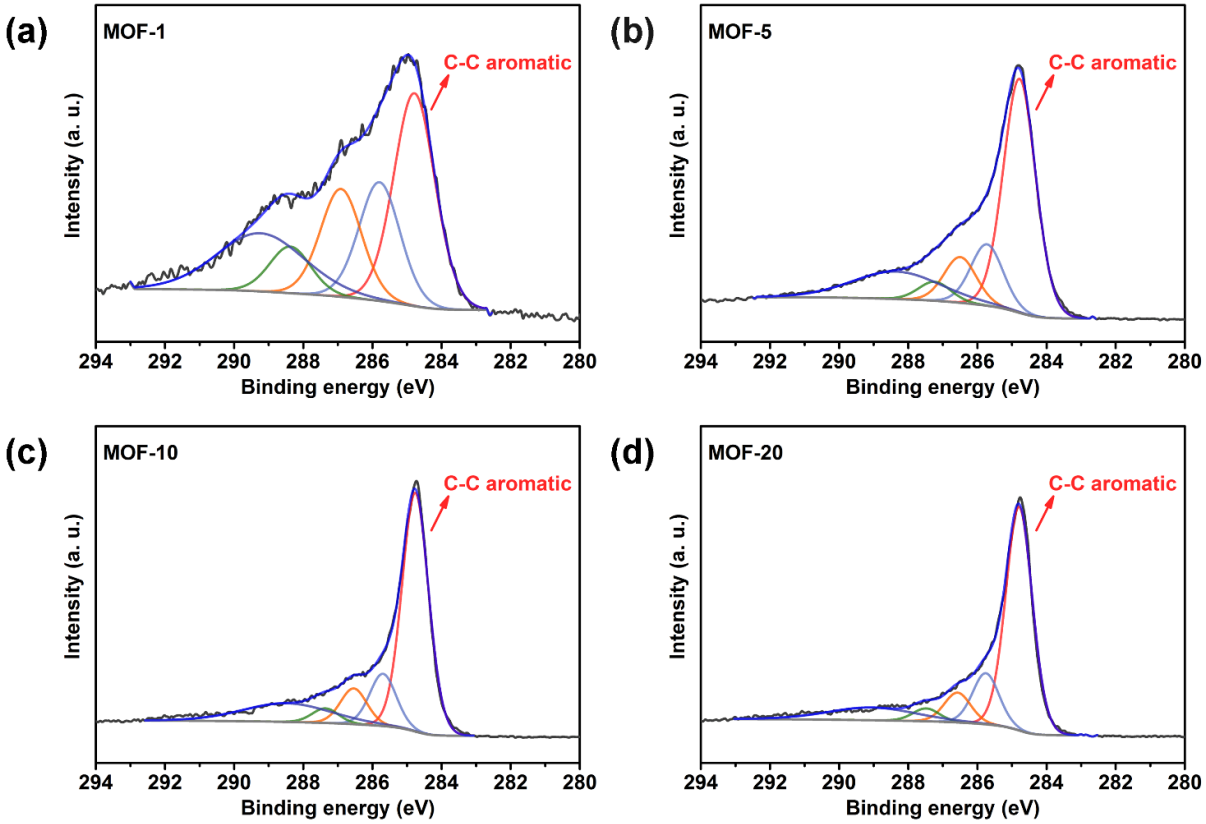


**Figure 5-4.** XPS C 1s spectra of (a) MOF-1, (b) MOF-5, (c) MOF-10 and (d) MOF-20.

**Table 5-1.** The peaks fitting results of C 1s core energy level for MOF/GO composites with different loading proportions.

| Binding energy (eV) | Bond assignment | MOF-1 (%) | MOF-5 (%) | MOF-10 (%) | MOF-20 (%) |
|---|---|---|---|---|---|
| 284.7 - 284.8 | C-C aromatic | 34.88 | 53.83 | 59.26 | 62.25 |
| 285.7 - 285.8 | C-C aliphatic | 19.45 | 14.12 | 12.94 | 14.21 |
| 286.5 - 286.9 | C-O | 17.66 | 10.51 | 8.86 | 8.27 |
| 287.2 - 288.6 | O=C-O | 7.63 | 4.36 | 3.60 | 3.57 |
| 288.4 - 289.3 | pi to pi* transition | 20.38 | 17.19 | 15.33 | 11.71 |

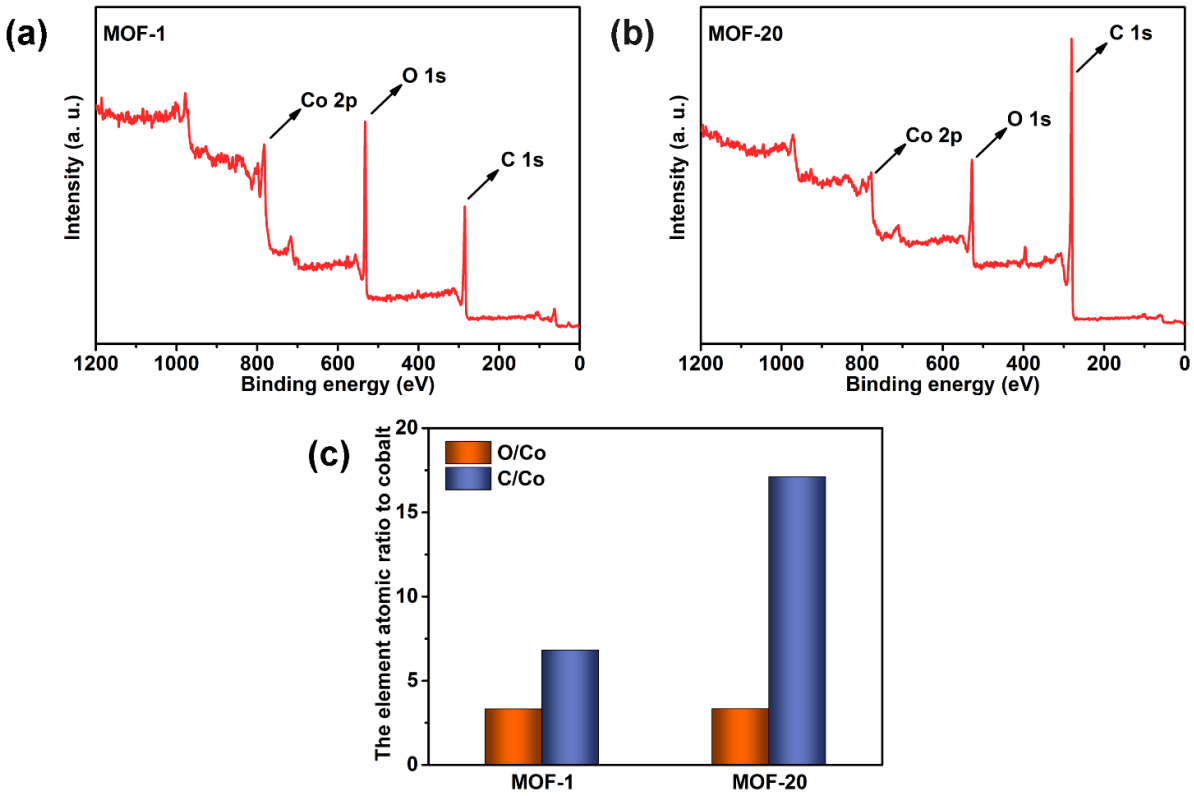


**Figure 5-5.** XPS survey spectra for (a) MOF-1 and (b) MOF-20. (c) The surface elements atomic ratios to Co measured by survey spectra.

The BET surface areas of the samples were calculated through testing their nitrogen sorption isotherms. As shown in Figure 5-6, the porosity increases initially with the increasing loading proportion of GO, among which MOF-5 exhibits the largest surface area (1634 $cm^2 g^{-1}$). Since GO has negligible porosity,[5d] this enhancement should be due to the formation of parallel interlayers that further expose the MOF surface and increase the micropore volume (as the ratio between micropore volume and total volume in Table 5-2).[96] In contrast, the overhigh amount of intercalated GO (larger than 10 wt%) would instead lead to a significant decrement of porosity, which is probably caused by the restacking of GO layers between the interlayers. This volcano trend demonstrates MOF as the primary contributor to the microporous structure of these composites.[5a]

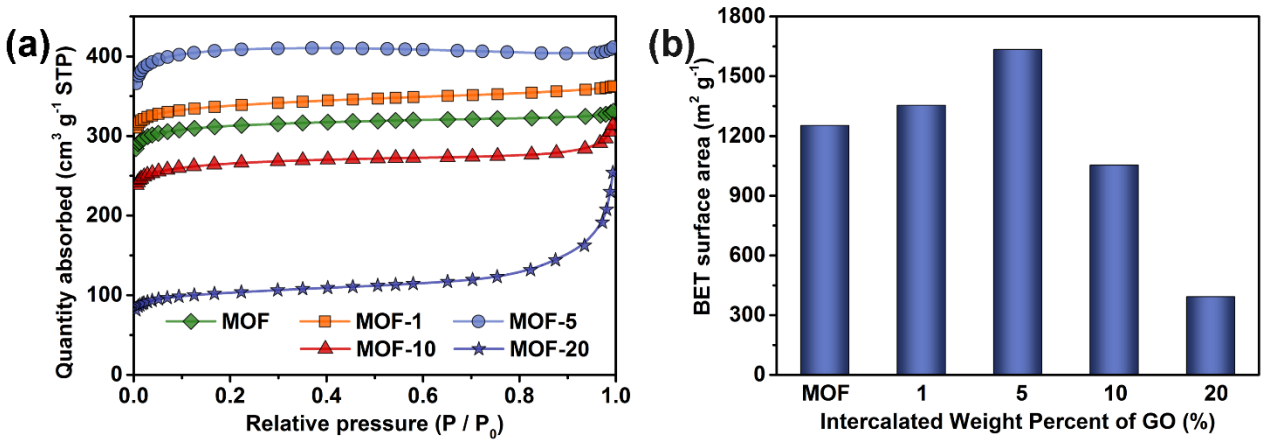


**Figure 5-6.** (a) Nitrogen sorption isotherms for MOF and MOF/GO composites with different loading proportions. (b) The surface areas estimated through Brunauer Emmett Teller (BET).

**Table 5-2.** Parameters of the porous structures calculated from nitrogen adsorption isotherms.

| Sample | $S_{BET}$ ($cm^2 g^{-1}$) | $V_{tot}$ ($cm^3 g^{-1}$) | $V_{micro}$ ($cm^3 g^{-1}$) | $V_{meso}$ ($cm^3 g^{-1}$) | $V_{micro}$ / $V_{tot}$ (%) |
|---|---|---|---|---|---|
| MOF | 1252 | 0.509 | 0.443 | 0.047 | 87.1 |
| MOF-1 | 1354 | 0.559 | 0.475 | 0.069 | 84.9 |
| MOF-5 | 1634 | 0.633 | 0.587 | 0.015 | 92.8 |
| MOF-10 | 1053 | 0.476 | 0.366 | 0.057 | 76.9 |
| MOF-20 | 392 | 0.366 | 0.120 | 0.222 | 32.7 |

In order to measure the OER activities of GO, MOF and MOF/GO composites, their linear sweep voltammetry (LSV) were tested with the scan rate of 10 mV $s^{-1}$ in 0.1 $_M$ KOH(Figure 5-7a). A closer look at the overpotential of 15 mA $cm^{-2}$ current density (Figure 5-7b) shows the linear tendency of OER activity, similarly through the mass activities at $\eta$ = 450 mV (Figure 5-7c). Obviously, all the composites have better performance compared with individual MOF or GO because of the synergistic effect between them. Due to the relatively low density and high conductivity of GO, even 1 wt% of GO in the composite (MOF-1) can substantially enhance the OER activity of the MOF. Among all the samples, MOF-20 exhibits the superior performance with the overpotential of 413 mV and the mass activity of 75.3 A $g^{-1}$ (without the aid of carbon black).

The electrochemical impedance spectroscopy (EIS) of samples are recorded at a constant potential of

1.63 V vs RHE under OER conditions. According to the Nyquist plots of EIS (Figure 5-7d), the charge transfer resistance of these composites have the same trend with their overpotential, which indicates the promotion of their charge transferability after intercalating GO. The low-frequency area of spectra (right end of each curve) shows a reduced resistance that was controlled by mass transfer instead of charge transfer. It is also notable that the trend of OER performance is different to the tendency of BET surface (Figure 5-6b). Therefore, electro-catalytic result confirms the major contribution of charge transferability instead of porosity to the improvement of OER activity for MOF/GO composites.

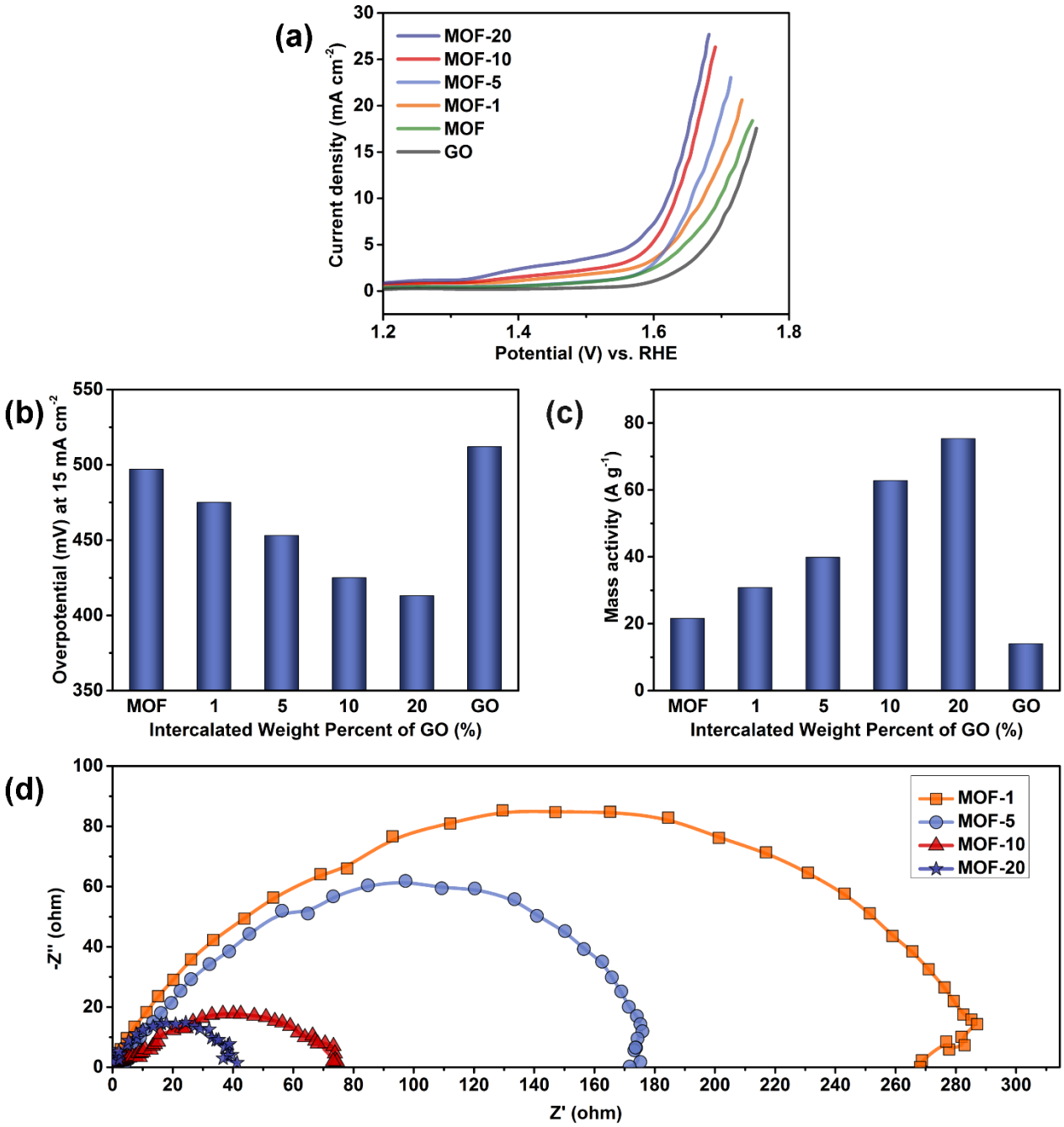


**Figure 5-7.** (a) Linear sweep voltammetry (LSV) curves for GO, MOF and MOF/GO composites with different loading proportions in 0.1 $_{M}$ KOH. (b) Overpotential of catalysts at current density of 15 mA cm$^{-2}$. (c) Mass activity at $\eta$ = 450 mV vs RHE. (d) Electrochemical impedance spectroscopy (EIS) analysis of catalysts at a constant potential of 1.63 V vs RHE.

## 5.3. Conclusion

Co-MOF-74/GO composites were successfully synthesised through intercalation GO into the MOF bulk phase during the synthesis process. Their hierarchical structures are clearly evidenced by XRD, XPS, SEM, and nitrogen sorption isotherms. This practical synthesis route is also confirmed by previous researches.[97] The suitable proportion of intercalated GO (equal or less than 5 wt%) can increase the porosity and promote the charge transferability of composite, so as to enhance its OER activity; while the overhigh amount of GO would lead to the restacking of layers, followed by BET decreasing. However, as the major contributor to the improvement of OER activity, charge transferability plays the crucial role instead of porosity for MOF/GO composites. Consequently, MOF-20 can achieve the optimal OER activity. It presents the lowest overpotential of 413 mV at 15 mA $cm^{-2}$ and the highest mass activity of 75.3 A $g^{-1}$ at $\eta$ = 450 mV (without the aid of carbon black) among all the catalysts in this study and clearly outperforms the pristine MOF. Their hierarchical layered structures have the potential to be developed as the major contributor in electro-catalysis, gas sorption, and supercapacitor, etc.

# Chapter 6. Conclusion and Recommendations

## 6.1. Conclusion

As mentioned above, the global environmental issues and growing energy demand can be relieved by the development of hydrogen energy. In terms of hydrogen production, the high-performance and cost-effective catalysts are highly desired for the sluggish half-reaction (OER). MOFs have great potential on the application of electro-catalysis for OER, owing to the earth-abundant and atomically dispersed metal centres. More importantly, the limitations based on their intrinsic properties can be exceeded through various processes strategies, and thus they can be utilised with the advantages of both homogeneous and heterogeneous catalysts. This project focuses on the designing of MOF-based electrocatalysts and the understanding of processes mechanism, so that MOFs' microstructure can be tuned delicately for superior activity toward OER. According to the presented studies, the following conclusions can be drawn:

(a) In regard to the full coordination of metal centres in MOFs, microwave-induced plasma can be applied to fine-tune CUMSs on Co-MOF-74 surface through designed conditions. The interaction is demonstrated as engraving effect, which is able to control the introduction of organic ligand defects with exposed metal sites. The quantitative correlation between CUMSs enrichment and electro-catalytic activity is revealed in order to understand the defect engineering profoundly.

(b) As to the low electronic conductivity of MOFs, GO can be intercalated in bulk Co-MOF-74 that synthesise the composites with the hierarchical structure. The parallel interlayers of GO are characterised that build conductive channels within MOF. The composites retain crystalline and porosity of MOF at relatively low proportion of GO, while improving charge transferability and OER activity at high loading percentage. The MOF-20 with optimal proportion exhibits the highest mass activity (75.3 A $g^{-1}$ at $\eta$ = 450 mV in 0.1 M KOH without the aid of carbon black) among all the samples in this part, which is three times larger than pristine MOF (21.6 A $g^{-1}$).

In summary, the extensive researches of plasma engraving and GO intercalation in this thesis reveal the promising methods for further tuning the microstructure of MOF based materials. The well-organised structures and particular electrochemical properties of MOFs are able to be utilised

efficiently. As a result, the earth-abundant metals have the potential to perform outstanding OER activity even compared with commercial noble catalysts.

## 6.2. Recommendations

The following recommendations are proposed for future researches:

(a) The universality of presented methods should be proved. It is noticeable that each type of MOF has a unique structure and coordination geometry. In order to develop the designing of strategies, various MOFs with different earth-abundant metals should be investigated through the process to detect their practical and enhanced results. The other MOFs with fully-coordination may be further tuned by plasma engraving, while their relatively large particle sizes are prospectively reduced by intercalated GO while exposing the internal surface.

(b) The precise control of bimetallic or multi-metallic MOFs should be taken for derived-catalysts toward OER. Their synergistic effect usually leads to unpredictable morphology and structural defects that have positive functions in electro-catalysis. Nevertheless, it is still an obstacle to clearly understand the interaction between different metal centres. In order to take the benefits, it might be valuable to achieve the application of derived strategies on bimetallic or multi-metallic MOFs.

(c) The stability of MOF as the electrochemical catalysts should be investigated under various electrolyte and voltage conditions. The reveal of reaction mechanism also needs more fundamental studies to further clarify the active sites, reaction pathway and MOF structure integrity.

(d) Even the availabilities of these routes were proved, more advanced characterisation (e.g., in-suit XAS) might still be recommended to perform in order to accomplish the integrated data support.

# References


[1] W. Wang, X. Xu, W. Zhou, Z. Shao, *Adv. Sci.* **2017**, 4, 1600371.

[2] a) J. Lee, J. H. Kwak, W. Choe, *Nat. Commun.* **2017**, 8, 14070; b) T. Wang, L. Gao, J. Hou, S. J. A. Herou, J. T. Griffiths, W. Li, J. Dong, S. Gao, M. M. Titirici, R. V. Kumar, A. K. Cheetham, X. Bao, Q. Fu, S. K. Smoukov, *Nat. Commun.* **2019**, 10, 1340.

[3] a) W. T. Hong, M. Risch, K. A. Stoerzinger, A. Grimaud, J. Suntivich, Y. Shao-Horn, *Energy Environ. Sci.* **2015**, 8, 1404; b) Y. Zheng, Y. Jiao, M. Jaroniec, S. Z. Qiao, *Angew. Chem. Int. Ed.* **2015**, 54, 52.

[4] M. Tahir, L. Pan, F. Idrees, X. Zhang, L. Wang, J.-J. Zou, Z. L. Wang, *Nano Energy* **2017**, 37, 136.

[5] a) N. A. Travlou, K. Singh, E. Rodríguez-Castellón, T. J. Bandosz, *J. Mater. Chem. A* **2015**, 3, 11417; b) J. A. Greathouse, M. D. Allendorf, *J. Am. Chem. Soc.* **2006**, 128, 13312; c) C. Petit, T. J. Bandosz, *Adv. Mater.* **2009**, 21, 4753; d) M. Seredych, C. Petit, A. V. Tamashausky, T. J. Bandosz, *Carbon* **2009**, 47, 445.

[6] Y. J. Tang, M. R. Gao, C. H. Liu, S. L. Li, H. L. Jiang, Y. Q. Lan, M. Han, S. H. Yu, *Angew. Chem. Int. Ed.* **2015**, 54, 12928.

[7] a) J. A. Villajos, G. Orcajo, C. Martos, J. Á. Botas, J. Villacañas, G. Calleja, *Int. J. Hydrogen Energy* **2015**, 40, 5346; b) C. Yan, H. Li, Y. Ye, H. Wu, F. Cai, R. Si, J. Xiao, S. Miao, S. Xie, F. Yang, Y. Li, G. Wang, X. Bao, *Energy Environ. Sci.* **2018**, 11, 1204; c) Y. Yang, L. Zhuang, R. Lin, M. Li, X. Xu, T. E. Rufford, Z. Zhu, *J. Power Sources* **2017**, 349, 68; d) Z. Chen, L. Cai, X. Yang, C. Kronawitter, L. Guo, S. Shen, B. E. Koel, *ACS Catal.* **2018**, 8, 1238.

[8] Z.-F. Huang, J. Song, K. Li, M. Tahir, Y.-T. Wang, L. Pan, L. Wang, X. Zhang, J.-J. Zou, *J. Am. Chem. Soc.* **2016**, 138, 1359.

[9] B. Y. Xia, Y. Yan, N. Li, H. B. Wu, X. W. Lou, X. Wang, *Nat. Energy* **2016**, 1, 15006.

[10] P. Pradip, S. Dhanraj, M. Mainak, X. Qiang, *Nat. Chem.* **2016**, 8, 718.

[11] a) J. Rossmeisl, A. Logadottir, J. K. Nørskov, *Chem. Phys.* **2005**, 319, 178; b) S. Zhao, Y. Wang,

J. Dong, C. T. He, H. Yin, P. An, K. Zhao, X. Zhang, C. Gao, L. Zhang, J. Lv, J. Wang, J. Zhang, A. M. Khattak, N. A. Khan, Z. Wei, S. Liu, H. Zhao, Z. Tang, *Nat. Energy* **2016**, 1, 16184; c) W. Xia, A. Mahmood, R. Zou, Q. Xu, *Energy Environ. Sci.* **2015**, 8, 1837.

[12] M. Zhao, Q. Lu, Q. Ma, H. Zhang, *Small Methods* **2017**, 1, 1600030.

[13] D. Zhang, H. Shi, R. Zhang, Z. Zhang, N. Wang, J. Li, B. Yuan, H. Bai, J. Zhang, *RSC Adv.* **2015**, 5, 58772.

[14] L. Tao, C.-Y. Lin, S. Dou, S. Feng, D. Chen, D. Liu, J. Huo, Z. Xia, S. Wang, *Nano Energy* **2017**, 41, 417.

[15] M. Zhao, K. Yuan, Y. Wang, G. Li, J. Guo, L. Gu, W. Hu, H. Zhao, Z. Tang, *Nature* **2016**, 539, 76.

[16] A. J. Clough, J. W. Yoo, M. H. Mecklenburg, S. C. Marinescu, *J. Am. Chem. Soc.* **2015**, 137, 118.

[17] R. R. Brooks, *Noble metals and biological systems : their role in medicine, mineral exploration, and the environment*, CRC Press, Baco Raton, Fla. **1992**.

[18] Y. Pi, N. Zhang, S. Guo, J. Guo, X. Huang, *Nano Lett.* **2016**, 16, 4424.

[19] a) F. I. Mattos-Costa, P. de Lima-Neto, S. A. S. Machado, L. A. Avaca, *Electrochim. Acta* **1998**, 44, 1515; b) J. Rossmeisl, Z. W. Qu, H. Zhu, G. J. Kroes, J. K. Nørskov, *J. Electroanal. Chem.* **2007**, 607, 83.

[20] T. Reier, M. Oezaslan, P. Strasser, *ACS Catal.* **2012**, 2, 1765.

[21] N.-I. Kim, Y. J. Sa, S.-H. Cho, I. So, K. Kwon, S. H. Joo, J.-Y. Park, *J. Electrochem. Soc.* **2016**, 163, F3020.

[22] R. D. L. Smith, M. S. Prevot, R. D. Fagan, Z. Zhang, P. A. Sedach, M. K. J. Siu, S. Trudel, C. P. Berlinguette, *Science* **2013**, 340, 60.

[23] C.-W. Chen, C.-Y. Chiang, *Int. J. Hydrogen Energy* **2017**, 42, 29773.

[24] a) Y. Zhu, W. Zhou, J. Sunarso, Y. Zhong, Z. Shao, *Adv. Funct. Mater.* **2016**, 26, 5862; b) J. Kim, X. Yin, K.-C. Tsao, S. Fang, H. Yang, *J. Am. Chem. Soc.* **2014**, 136, 14646; c) J. Suntivich, K. J. May, H. A. Gasteiger, J. B. Goodenough, Y. Shao-Horn, *Science* **2011**, 334, 1383; d) Y. Miyahara, K.

Miyazaki, T. Fukutsuka, T. Abe, *Chem. Commun.* **2017**, 53, 2713.

[25] J. Ryu, N. Jung, J. H. Jang, H. J. Kim, S. J. Yoo, *ACS Catal.* **2015**, 5, 4066.

[26] Y. P. Zhu, Y. P. Liu, T. Z. Ren, Z. Y. Yuan, *Adv. Funct. Mater.* **2015**, 25, 7337.

[27] A. Dutta, N. Pradhan, *J. Phys. Chem. Lett.* **2017**, 8, 144.

[28] J. Chang, Y. Xiao, M. Xiao, J. Ge, C. P. Liu, W. Xing, *ACS Catal.* **2015**, 5, 6874.

[29] C.-C. Hou, S. Cao, W.-F. Fu, Y. Chen, *ACS Appl. Mat. Interfaces* **2015**, 7, 28412.

[30] Y. Yan, B. Zhao, S. C. Yi, X. Wang, *J. Mater. Chem. A* **2016**, 4, 13005.

[31] Y. Li, P. Hasin, Y. Wu, *Adv. Mater.* **2010**, 22, 1926.

[32] P. Chen, K. Xu, Z. Fang, Y. Tong, J. Wu, X. Lu, X. Peng, H. Ding, C. Wu, Y. Xie, *Angew. Chem. Int. Ed.* **2015**, 54, 14710.

[33] Y. Zhang, B. Ouyang, J. Xu, G. Jia, S. Chen, R. S. Rawat, H. J. Fan, *Angew. Chem. Int. Ed.* **2016**, 55, 8670.

[34] Y.-T. Pi, X.-Y. Xing, L.-M. Lu, Z.-B. He, T.-Z. Ren, *RSC Adv.* **2016**, 6, 102422.

[35] T. Odedairo, J. Ma, Y. Gu, W. Zhou, J. Jin, X. S. Zhao, Z. Zhu, *Nanotechnology* **2014**, 25, 495604.

[36] B. Nohra, H. El Moll, L. M. Rodriguez Albelo, P. Mialane, J. Marrot, C. Mellot-Draznieks, M. O'Keeffe, R. Ngo Biboum, J. Lemaire, B. Keita, L. Nadjo, A. Dolbecq, *J. Am. Chem. Soc.* **2011**, 133, 13363.

[37] K. Shen, X. Chen, J. Chen, Y. Li, *ACS Catal.* **2016**, 6, 5887.

[38] N. Stock, S. Biswas, *Chem. Rev.* **2012**, 112, 933.

[39] A. Rabenau, *Angew. Chem. Int. Ed.* **1985**, 24, 1026.

[40] T. Grant Glover, G. W. Peterson, B. J. Schindler, D. Britt, O. Yaghi, *Chem. Eng. Sci.* **2011**, 66, 163.

[41] K.-Y. A. Lin, H.-A. Chang, *J. Taiwan Inst. Chem. Eng.* **2015**, 53, 40.

[42] Q. Qian, Y. Li, Y. Liu, L. Yu, G. Zhang, *Adv. Mater.* **2019**, 31, 1901139.

[43] a) S. Biswas, M. Grzywa, H. P. Nayek, S. Dehnen, I. Senkovska, S. Kaskel, D. Volkmer, *Dalton Trans.* **2009**, , 6487; b) P. Horcajada, T. Chalati, C. Serre, B. Gillet, C. Sebrie, T. Baati, J. F. Eubank, D. Heurtaux, P. Clayette, C. Kreuz, J. S. Chang, Y. K. Hwang, V. Marsaud, P. N. Bories, L. Cynober, S. Gil, G. Ferey, P. Couvreur, R. Gref, *Nat. Mater.* **2010**, 9, 172; c) N. A. Khan, E. Haque, S. H. Jhung, *PCCP* **2010**, 12, 2625.

[44] S. H. Jhung, J. H. Lee, J. Chang, *Microwave Synthesis of a Nanoporous Hybrid Material, Chromium Trimesate*, The Korean Chemical Society, Seoul **2005**.

[45] M. Schlesinger, S. Schulze, M. Hietschold, M. Mehring, *Microporous Mesoporous Mater.* **2010**, 132, 121.

[46] U. Mueller, M. Schubert, F. Teich, H. Puetter, K. Schierle-Arndt, J. Pastré, *J. Mater. Chem.* **2006**, 16, 626.

[47] M. Hartmann, S. Kunz, D. Himsl, O. Tangermann, S. Ernst, A. Wagener, *Langmuir* **2008**, 24, 8634.

[48] a) J. B. Lin, R. B. Lin, X. N. Cheng, J. P. Zhang, X. M. Chen, *Chem. Commun.* **2011**, 47, 9185; b) W. Yuan, A. L. Garay, A. Pichon, R. Clowes, C. D. Wood, A. I. Cooper, S. L. James, *CrystEngComm* **2010**, 12.

[49] A. Pichon, A. Lazuen-garay, S. L. James, *CrystEngComm* **2006**, 8, 211.

[50] a) J. H. Bang, K. S. Suslick, *Adv. Mater.* **2010**, 22, 1039; b) T. Mason, D. Peters, *Practical Sonochemistry: Power Ultrasound Uses and Applications*, Woodhead Publishing, **2002**.

[51] L. G. Qiu, Z. Q. Li, Y. Wu, W. Wang, T. Xu, X. Jiang, *Chem. Commun.* **2008**, , 3642.

[52] D. W. Jung, D. A. Yang, J. Kim, J. Kim, W. S. Ahn, *Dalton Trans.* **2010**, 39, 2883.

[53] G. Hai, X. Jia, K. Zhang, X. Liu, Z. Wu, G. Wang, *Nano Energy* **2018**, 44, 345.

[54] J. Duan, S. Chen, C. Zhao, *Nat. Commun.* **2017**, 8, 15341.

[55] M. Zhao, Y. Wang, Q. Ma, Y. Huang, X. Zhang, J. Ping, Z. Zhang, Q. Lu, Y. Yu, H. Xu, Y. Zhao, H. Zhang, *Adv. Mater.* **2015**, 27, 7372.

[56] L. Cao, Z. Lin, F. Peng, W. Wang, R. Huang, C. Wang, J. Yan, J. Liang, Z. Zhang, T. Zhang, L.

Long, J. Sun, W. Lin, *Angew. Chem. Int. Ed.* **2016**, 55, 4962.

[57] a) M. Zhao, Y. Huang, Y. Peng, Z. Huang, Q. Ma, H. Zhang, *Chem. Soc. Rev.* **2018**, 47, 6267; b) P. Amo-Ochoa, L. Welte, R. González-Prieto, P. J. Sanz Miguel, C. J. Gómez-García, E. Mateo-Martí, S. Delgado, J. Gómez-Herrero, F. Zamora, *Chem. Commun. (Cambridge, U. K.)* **2010**, 46, 3262.

[58] Y. Peng, Y. Li, Y. Ban, H. Jin, W. Jiao, X. Liu, W. Yang, *Science* **2014**, 346, 1356.

[59] H. B. Wu, X. W. Lou, *Sci. Adv.* **2017**, 3, eaap9252.

[60] L. Han, X. Y. Yu, X. W. Lou, *Adv. Mater.* **2016**, 28, 4601.

[61] J. d. L. Fuente, Graphene Oxide - What Is It?, https://www.graphenea.com/pages/graphene-oxide#.WpX84ehuaUm, accessed: March, 2019.

[62] a) J. d. L. Fuente, Graphene Applications & Uses, https://www.graphenea.com/pages/graphene-properties#.WpZUpuhuaUk, accessed: March, 2019; b) L. Yan, H. Jiang, Y. Xing, Y. Wang, D. Liu, X. Gu, P. Dai, L. Li, X. Zhao, *J. Mater. Chem. A* **2018**, 6, 1682; c) L. Yang, B. Tang, P. Wu, *J. Mater. Chem. A* **2015**, 3, 15838.

[63] M. Jahan, Z. Liu, K. P. Loh, *Adv. Funct. Mater.* **2013**, 23, 5363.

[64] H. X. Zhong, J. Wang, Y. W. Zhang, W. L. Xu, W. Xing, D. Xu, Y. F. Zhang, X. B. Zhang, *Angew. Chem. Int. Ed.* **2014**, 53, 14235.

[65] T. Y. Ma, S. Dai, M. Jaroniec, S. Z. Qiao, *J. Am. Chem. Soc.* **2014**, 136, 13925.

[66] D. Sun, L. Ye, F. Sun, H. Garcia, Z. Li, *Inorg. Chem.* **2017**, 56, 5203.

[67] K. Wang, Y. Chen, R. Tian, H. Li, Y. Zhou, H. Duan, H. Liu, *ACS Appl. Mat. Interfaces* **2018**, 10, 11333.

[68] I. Khan, A. Badshah, N. Haider, S. Ullah, D. Anjum, M. Nadeem, *J. Solid State Electrochem.* **2014**, 18, 1545.

[69] Q. Z. Luo, N. D'angelo, R. L. Merlino, *Phys. Plasmas* **1998**, 5, 2868.

[70] J. B. Decoste, G. W. Peterson, M. W. Smith, C. A. Stone, C. R. Willis, *J. Am. Chem. Soc.* **2012**, 134, 1486.

[71] J. B. Decoste, J. A. Rossin, G. W. Peterson, *Chemistry* **2015**, 21, 18029.

[72] S. Dissegna, K. Epp, W. R. Heinz, G. Kieslich, R. A. Fischer, *Adv. Mater.* **2018**, 30, e1704501.

[73] L. Xu, Q. Jiang, Z. Xiao, X. Li, J. Huo, S. Wang, L. Dai, *Angew. Chem. Int. Ed.* **2016**, 55, 5277.

[74] T. Odedairo, J. Chen, Z. Zhu, *J. Phys. Chem. C* **2013**, 117, 21288.

[75] M. Witman, S. Ling, S. Anderson, L. Tong, K. C. Stylianou, B. Slater, B. Smit, M. Haranczyk, *Chem. Sci.* **2016**, 7, 6263.

[76] S. Gao, B. S. Villacorta, L. Ge, T. E. Rufford, Z. Zhu, *Carbon* **2017**, 124, 142.

[77] S. Gao, L. Ge, T. E. Rufford, Z. Zhu, *Microporous Mesoporous Mater.* **2017**, 238, 19.

[78] H. Wu, X. Lou, *Sci. Adv.* **2017**, 3, eaap9252.

[79] X.-F. Lu, P.-Q. Liao, J.-W. Wang, J.-X. Wu, X.-W. Chen, C.-T. He, J.-P. Zhang, G.-R. Li, X.-M. Chen, *J. Am. Chem. Soc.* **2016**, 138, 8336.

[80] K. Rui, G. Zhao, Y. Chen, Y. Lin, Q. Zhou, J. Chen, J. Zhu, W. Sun, W. Huang, S. X. Dou, *Adv. Funct. Mater.* **2018**, 28, 1801554.

[81] a) S. Chui, S. Lo, J. Charmant, A. Orpen, I. Williams, *Science* **1999**, 283, 1148; b) N. L. Rosi, J. Kim, M. Eddaoudi, B. Chen, M. O'Keeffe, O. M. Yaghi, *J. Am. Chem. Soc.* **2005**, 127, 1504.

[82] B. David, F. Hiroyasu, W. Bo, T. G. Glover, M. Y. Omar, *PNAS* **2009**, 106, 20637.

[83] Z. Wang, Y. Zhang, E. C. Neyts, X. Cao, X. Zhang, B. W. L. Jang, C.-j. Liu, *ACS Catal.* **2018**, 8, 2093.

[84] a) J. Musil, *Vacuum* **1986**, 36, 161; b) S. Keizo, O. Sadayuki, S. Noriyuki, K. Ichiro, *Jpn. J. Appl. Phys.* **1977**, 16, 1979.

[85] a) J. Weber, *Physica B* **1991**, 170, 201; b) N. M. P. Johnson, F. A. Ponce, R. A. Street, R. J. Nemanich, *Phys. Rev. B* **1987**, 35, 4166; c) I. Umezu, K. Kohno, K. Aoki, Y. Kohama, A. Sugimura, M. Inada, *Vacuum* **2002**, 66, 453.

[86] a) P. D. C. Dietzel, Y. Morita, R. Blom, H. Fjellvåg, *Angew. Chem. Int. Ed.* **2005**, 44, 6354; b) H. Jiang, Q. Wang, H. Wang, Y. Chen, M. Zhang, *ACS Appl. Mat. Interfaces* **2016**, 8, 26817.

[87] a) L. Zhuang, L. Ge, Y. Yang, M. Li, Y. Jia, X. Yao, Z. Zhu, *Adv. Mater.* **2017**, 29, 1606793; b) L. Ge, W. Zhou, V. Rudolph, Z. Zhu, *J. Mater. Chem. A* **2013**, 1, 6350.

[88] S. Luo, J. Wang, *Environ. Sci. Pollut. Res. Int.* **2018**, 25, 5521.

[89] C. D. Scott, S. Farhat, A. Gicquel, K. Hassouni, *J. Thermophys Heat Transfer* **1996**, 10, 426.

[90] *J. Chem. Educ.* **1993**, 70, A25.

[91] X. Wang, L. Zhuang, Y. Jia, H. Liu, X. Yan, L. Zhang, D. Yang, Z. Zhu, X. Yao, *Angew. Chem. Int. Ed.* **2018**, 57, 16421.

[92] Q. Jiang, Z. Li, S. Wang, H. Zhang, *RSC Adv.* **2015**, 5, 92995.

[93] E. Herbst, *Philos. Trans. R. Soc. London, Ser. A* **2000**, 358, 2523.

[94] B. Han, D. Qian, M. Risch, H. Chen, M. Chi, Y. S. Meng, Y. Shao-Horn, *J. Phys. Chem. Lett.* **2015**, 6, 1357.

[95] J.-Q. Shen, P.-Q. Liao, D.-D. Zhou, C.-T. He, J.-X. Wu, W.-X. Zhang, J.-P. Zhang, X.-M. Chen, *J. Am. Chem. Soc.* **2017**, 139, 1778.

[96] C. Petit, J. Burress, T. J. Bandosz, *Carbon* **2011**, 49, 563.

[97] a) L. Ge, Y. Yang, L. Wang, W. Zhou, R. De Marco, Z. Chen, J. Zou, Z. Zhu, *Carbon* **2015**, 82, 417; b) Y. Yang, L. Ge, V. Rudolph, Z. Zhu, *Dalton Trans.* **2014**, 43, 7028; c) R. Lin, L. Ge, H. Diao, V. Rudolph, Z. Zhu, *J. Mater. Chem. A* **2016**, 4, 6084.